

THE OSAKA UNIVERSITY
GRADUATE SCHOOL OF SCIENCE
TOYONAKA, OSAKA

⁴⁰Ca - ⁴⁰Ar MASS DIFFERENCE MEASUREMENT
BY HIGH RESOLUTION MASS SPECTROMETER

by

Sadayoshi FUKUMOTO

Submitted to the Faculty of Science
in partial fulfillment of the requirements
for the degree of
Doctor of Philosophy

OSAKA UNIVERSITY

1967

Contents

1. Introduction	1
2. Principle of High Resolution Mass Spectrometer	6
2.1. Behavior of charged particles in the r^{-1} type magnetic field	6
2.2. Principle of magnetic analyzer with very large dispersion	10
2.3. Design	13
2.4. Second order consideration	15
3. Construction of High Resolution Mass Spectrometer	18
3.1. Dispersing or r^{-1} magnetic field	18
3.2. Energy selector	19
3.3. Focusing magnet	20
3.4. Ion source	21
3.5. Objective slit system	21
3.6. Detector	22
3.7. Vacuum system	22
3.8. Alignment of the apparatus	23
3.9. Reduction of stray magnetic field	24
4. Artificial Multiplets of ^{39}K	26
5. Modifications and Improvements of the Apparatus	30
5.1. Electron multiplier detection system	30
5.2. Beam scanner	31
5.3. Ion pump	31
5.4. The effect of 60 Hz hum magnetic field	32
5.5. Modification of the ion source	32
5.6. Beam emittance	33

6.	Preliminary Peak Matching Measurement	36
6.1.	Principle of the peak matching method	36
6.2.	Experimental preparation	38
6.3.	Energy focusing	39
6.4.	Direction focusing	40
6.5.	Results	40
7.	⁴⁰ Ca - ⁴⁰ Ar Mass Difference	43
8.	Concluding Remarks	46
	Acknowledgments	48
	References	49
	Appendix	51
	List of Tables	57
	List of Figures	58

1. Introduction

The atomic mass is one of the most important physical quantities and its precise determination has been accomplished in the past by many investigators with the latest methods and techniques. The atomic mass can be determined by several ways, among these two methods are widely adopted, one is the calculation based on the nuclear reaction energies and the other is the mass spectroscopic method. It may be probable in the highly precise measurements that the minute discrepancies may exist among the observed values obtained in the different experiments. However, in 1961, the situation was not so favourable for the mass-spectroscopists.

In 1960 and 1961, a list of atomic masses based on experimental data was published by E. Everling, L. A. König, J. H. E. ¹ Mattauch and A. H. Wapstra. The mass values in the table were calculated by the least squares adjustment of enormous experimental data from mass doublet and nuclear Q-value measurements. In this work, they found it to be a good policy to multiply all errors in the mass doublet measurements by the "consistency factor" 2.65 in order to get consistent mass values. This means that the accuracy of the mass values by mass-spectroscopists would not be so good as indicated by the probable errors quoted in the experimental results. Mattauch et al. defined the errors quoted in the experimental data as internal errors and those of adjusted values as external errors.

There may be many reasons which cause such a situation. Among these, probably the most important one is that the

resolving powers of the machines used are not enough to calculate the result to such an extent of significant figures. Up to 1960, the resolving powers of the available apparatus were less than 10^5 except for some testing cases, here the resolving power means the value of a mass M divided by narrowly detectable mass increment ΔM . On the other hand, the errors quoted to the observed mass values were, for example, 2 micro-u to the mass of ^{16}O obtained by the photographic plate² and 3 micro-u to ^{84}Sr obtained by the so-called peak matching method.³

The internal errors are distributed over a range of about 10^{-2} to 10^{-3} of the mass peak width. If the assumption that the two species of the ions which constitute the mass doublet have the same distribution function in the 6-dimensional phase space at the exit of the ion source is not fulfilled, some systematic errors may be introduced into the measured mass values.⁴

The peak matching method⁵ is now widely adopted in many laboratories because it has some merits compared with the photographic plate detection system. In the peak matching method, ions of two components of mass doublet are detected electronically and their mass spectrum is displayed on a oscilloscope screen. It enables an easy and quick measurement of the distance between mass peaks of the doublet, and furthermore, the adjustment of focusing can be easily done observing the peak shape on the oscilloscope screen.

When the peak matching technique is used, it is difficult to confirm that the two mass peaks match so precisely as mentioned above on the screen, and this fact introduces another

possibility for error. Fortunately, this type of error is greatly reduced by the somewhat sophisticated method which uses a multi-channel memory system in conjunction with the electron multiplier detector. At any rate, it seems very difficult to determine the atomic mass to the order of 10^{-2} - 10^{-3} of the peak width.

The most straightforward solution will be the improvement of the resolving power of the mass spectrometer, and many efforts have been done to establish the higher dispersion and resolution. If the apparatus is enlarged linearly except for the slit system, then the resolving power is expected to increase proportionally to the linear dimensions of the apparatus. During the past ten years, a number of large apparatus have been constructed, and a resolving power of several hundred thousand has been obtained. ^{7,8,9,10,11,12,13,14,15}

The consistency factors have been also improved from ¹⁶ 2.65 to 1.5 for the most favorable cases. It seems, however, very difficult to enlarge the linear dimensions of the apparatus still more to increase the resolving power about one order of magnitude because of economic and technical reasons. Moreover, the brightness of the ion optical system is much reduced by enlarging the ordinary double focusing apparatus which has the cylindrical electric field and the homogeneous magnetic field. This contradicts the requirement that the brighter system is necessary for the precise measurements.

A new method has been proposed which is very attractive for two reasons. ¹⁷ First, it can increase the resolving power and the mass dispersion about one order of magnitude while the

linear dimension of the machine is only somewhat larger than the ordinary one. Second, it can produce the focusing actions not only in r-direction but also in z-direction so that the brightness of the system is almost kept unchanged. It is the essential feature of this new method to use a mass dispersing field which has no lens action.

A relatively small apparatus is constructed which has a r^{-1} magnetic field as the dispersing field together with a toroidal electric field and an uniform magnetic field as the focusing fields. In Table 1, there are some characteristic parameters of our high resolution mass spectrometer and typical ordinary double focusing machines.

In the 1964 mass table, atomic masses and binding energies of ^{40}Ar and ^{40}Ca are given as

^{40}Ar	$39,962,384.2 \pm 0.8$	μu	$343,811.7 \pm 2.7$	keV
^{40}Ca	$39,962,588.9 \pm 3.5$	μu	$342,056.2 \pm 4.3$	keV

The mass difference between them is very small. To separate such a narrow mass doublet, it is necessary to construct a high resolution mass spectrometer which has a resolving power equal to or greater than 2×10^5 at the base of the mass peak. This means a resolving power of 4×10^5 at the half-height of the peak. From the difficulty in actualizing such a high resolving power, it has not yet been done to measure the direct mass difference of ^{40}Ar and ^{40}Ca , although they are very abundant elements in nature. According to 1964 atomic mass table, the error assigned to the mass of ^{40}Ar is only 0.8 micro-u, whereas the error to ^{40}Ca is about five times of the former. If the mass difference $^{40}\text{Ca} - ^{40}\text{Ar}$ is measured accurately enough, then the mass of ^{40}Ca can be estimated more accurately by

combining the mass difference with the mass of ^{40}Ar . This also enables the estimation of the reliability of the 1964 mass table.

This paper describes the design and construction of the new high resolution mass spectrometer and the experiment on the direct measurement of the mass difference $^{40}\text{Ca} - ^{40}\text{Ar}$.

2. Principle of the High Resolution Mass Spectrometer

2.1. Behavior of charged particles in the r^{-1} type magnetic field

Many mass spectrometers ever built have installed the sector type magnets which produce uniform magnetic fields perpendicular to the planes of the ion trajectories. Ions which start from the source point are focused on the image point by this field. The locations of the magnetic field, the source and the image are determined by Barber's law(Fig.1).

According to the optical analogy, the sector type magnetic field has two functions simultaneously, one is the prismatic action or dispersion (with respect to ion momentum), and the other the lens action as mentioned above (Fig.2(a)). Unfortunately, each function is not controlled independently, and the coefficient of the dispersion at the image point can not exceed largely the radius of curvature of ion path in the magnetic field. In order to improve such a situation, let us consider the ion optical properties of the magnetic field (including non-uniform field) more generally.²⁰

We denote the optical axis of the system as the orbit of the ion which has mass m_0 and velocity v_0 . If we assume that the magnetic field has only the normal component to the median plane and has the same intensity along the optical axis, then the optical axis in the magnetic field should be a circle with the radius of curvature a . In order to express the position of the ion, the cylindrical coordinate system is introduced, the origin of which coincides with the center of the circular optical axis, z -axis being perpendicular to the median plane, so that r -vector is in it and φ increases as the ion travels.

If so-called paraxial rays are treated, ions travel near the optical axis and nearly parallel to it. If ρ and ζ are introduced by the relations:

$$r = a(1 + \rho), \quad z = a\zeta, \quad (2-1)$$

then

$$\rho \ll 1, \quad \zeta \ll 1. \quad (2-2)$$

The magnetic field in the median plane (the plane of geometrical symmetry) can be expanded as follows:

$$H_z(\rho, 0) = H_0(1 + n\rho + n_2\rho^2 + \dots). \quad (2-3)$$

Then, according to the Maxwell's equations, the magnetic field near the optical axis is expressed in the first order approximation as follows:

$$H_r(\rho, \zeta) = H_0 n \zeta, \quad (2-4)$$

$$H_z(\rho, \zeta) = H_0(1 + n\rho), \quad (2-5)$$

$$A_\varphi(\rho, \zeta) = \frac{aH_0}{2}(1 + \rho + n\rho^2 - n\zeta^2), \quad (2-6)$$

where H_r and H_z are r- and z-components of the magnetic field and A_φ the φ -component of the vector potential.

In general, the trajectory of the charged particle in the static magnetic field is determined by the variational expression²¹

$$\delta \int (P + e A_s) ds = 0, \quad (2-7)$$

where P is the magnitude of the momentum of the particle, e the charge, ds the line element and A_s the ds -component of the vector potential.

In the median plane, an ion which has mass $m = m_0(1 + \gamma)$

and velocity $v = v_0(1+\beta)$ passes along the orbit which is determined by the differential equation derived from Eq.(2-7):

$$\frac{d^2 \rho}{d\varphi^2} = -\mathcal{E}_r^2 (\rho - \delta) , \quad (2-8)$$

where

$$\mathcal{E}_r^2 = 1 + n , \quad (2-9)$$

$$\delta = (\gamma + \beta) / \mathcal{E}_r^2 . \quad (2-10)$$

In the first order approximation, the ion motion in the z-direction is not coupled with that of the r-direction and is given by

$$\frac{d^2 \zeta}{d\varphi^2} = -\mathcal{E}_z^2 , \quad (2-11)$$

where

$$\mathcal{E}_z^2 = -n \quad (2-12)$$

If $\mathcal{E}_r^2 > 0$ in Eq.(2-8), the ion oscillates around the optical axis in the median plane, and this is the case that happened in ordinary mass spectrometers. Provided \mathcal{E}_r^2 tends to zero, then Eq.(2-8) is reduced to

$$\frac{d^2 \rho}{d\varphi^2} = \delta' , \quad (2-13)$$

where

$$\delta' = (\gamma + \beta) . \quad (2-14)$$

The solution of Eq.(2-13) is

$$\rho = \alpha_r' \varphi + \frac{1}{2} \delta' \varphi^2 + \rho_1 , \quad (2-15)$$

where ρ_1 and α_r' are the normalized distance and the angle of the deviation from the optical axis at $\varphi = 0$.

The field has only the dispersing action but no focusing

action as shown in Eq.(2-15), so we call it the dispersing field.

If the strength of a magnetic field in the median plane is decreased inversely proportional to r , the field in the region $r \approx a$ is expressed by

$$H(r, \theta) = H_0 a/r = H_0 (1 - \rho + \rho^2) \quad (2-16)$$

Thus the magnetic field satisfies the condition $n = -1$, it turns $\mathcal{R}_r^2 = 0$. Therefore, the r^{-1} type magnetic field will be used as the dispersing field.

Now we consider a magnetic scalar potential in the region between coaxial equipotential cones. It is assumed that the relative permeability of the magnetic material is infinity. The equipotential surfaces are expressed by $\theta = \frac{\pi}{2} \pm \theta_0$ in a spherical polar coordinate system (r, θ, φ) . The scalar potential ϕ satisfies Laplace's equation:

$$\nabla^2 \phi = 0$$

The boundary condition is given by

$$\phi(\theta = \frac{\pi}{2} - \theta_0) = \phi_0, \quad \phi(\theta = \frac{\pi}{2} + \theta_0) = -\phi_0.$$

Then, the potential ϕ is given by

$$\phi = \phi_0 \frac{\log \tan(\frac{\pi}{4} - \frac{\chi}{2})}{\log \tan \frac{\chi_0}{2}}$$

where θ and θ_0 are replaced by χ and χ_0 as follows:

$$\chi = \frac{\pi}{2} - \theta, \quad \pm \chi_0 = \frac{\pi}{2} \mp \theta_0.$$

Then the magnetic field H_θ is expressed by

$$H_\theta = -\frac{1}{r} \frac{\partial \phi}{\partial \theta} = -\frac{\phi_0}{\log \tan \frac{\chi_0}{2}} \cdot \frac{1}{r \cos \chi}.$$

In the median plane where $\chi = 0$

$$H(r, 0) = - \frac{\phi_0}{\log \tan \frac{\chi_0}{2}} \cdot \frac{1}{r} \quad (2-17)$$

Therefore, when the pole gap of the magnet is much smaller than the radius of curvature a of the central beam, the r^{-1} type magnetic field can be produced by a magnetic pole having conical surfaces. If necessary, the r -dependence of the magnetic field may be modified by the adjustment of the pole gap. This feature of the field is quite satisfactory for practical application.

2.2. Principle of magnetic analyzer with very large dispersion

If we deal with the ion optics of the first order approximation and the case of normal entry and exit, the results may be summarised as follows.

Relationship between the ion source and the image position (Newton's equation):

$$(\ell' - g)(\ell'' - g) = f^2 \quad (2-8)$$

where ℓ' is the distance between the source and the entry field boundary (object distance) and ℓ'' the distance between the image and the exit field boundary (image distance).

Distance between the focus and the field boundary:

$$g = \frac{a}{\alpha_r} \cot \alpha_r \Phi \quad (2-9)$$

where Φ is the reflecting angle of the field.

Focal length:

$$f = \frac{a}{\alpha_r} \frac{1}{\sin \alpha_r \Phi} \quad (2-10)$$

Distance between the principal plane and the field boundary:

$$h = -\frac{a}{\partial e_r} \tan \frac{\partial_r \Phi}{2} \quad (2-21)$$

Image magnification:

$$X = \frac{f}{l' - g} = \frac{l'' - g}{f} \quad (2-22)$$

Dispersion at the image position:

$$D = a \delta \left(1 + \frac{f}{l' - g}\right) = a \delta (1 + X) \quad (2-23)$$

where

$$\delta = \frac{\gamma + \beta}{\partial e_r^2} \quad (2-24)$$

Focusing angle:

$$\alpha_r'' = -\frac{l' - g}{f} \alpha_r' = -\frac{\alpha_r'}{X} \quad (2-25)$$

The relations above mentioned are applicable not only to the magnetic field but also to the electric field in which the central ion has a circular trajectory. It is assumed that the electrostatic potential is given by

$$\phi(\rho, \xi) = -a E_0 \left\{ \rho + \frac{1}{2} l \rho^2 - \frac{1}{2} (1+l) \xi^2 \right\}$$

If ∂_{re} and δ_e are substituted for ∂_r and δ , where

$$\partial_{re}^2 = l + g$$

$$\delta_e = (\gamma + 2\beta) / \partial_{re}^2$$

then all the equations (2-18) to (2-25) express the ion optical properties of the electric field.

As already mentioned, the ordinary sector type field, used as a particle analyzer, has the focusing and the dispersing actions simultaneously. If it is divided in two parts at the plane where the ion beam becomes parallel, then the source and its image are located at the respective focal points of the divided sector fields. Let the deflecting angle of each

field be Φ_1 and Φ_3 as shown in Fig.2(b), then the focal lengths f_1 and f_3 are given by the following equations:

$$f_1 = \frac{a}{\partial \epsilon_r} \frac{1}{\sin \partial \epsilon_r \Phi_1} \quad (2-26)$$

$$f_3 = \frac{a}{\partial \epsilon_r} \frac{1}{\sin \partial \epsilon_r \Phi_3} \quad (2-27)$$

The dispersion at the image is given by

$$D_o = \left(\frac{a}{\partial \epsilon_r^2} \cdot \frac{1}{f_1} + \frac{a}{\partial \epsilon_r^2} \cdot \frac{1}{f_3} \right) f_3 \delta' \quad (2-28)$$

and the magnification of the image is f_3 / f_1 . If the objective slit width is s , the resolving power R_o of the ion optical system is given by

$$R_o = \left(\frac{a}{\partial \epsilon_r^2} \cdot \frac{1}{f_1} + \frac{a}{\partial \epsilon_r^2} \cdot \frac{1}{f_3} \right) \frac{f_1}{s} \quad (2-29)$$

Now, suppose that we separate these two fields and insert a dispersing field in between as shown in Fig.2(c), the deflecting angle being Φ_2 . This arrangement of the fields is quite analogous to the optical prism spectrometer shown in Fig.2(a). The divided fields act as focusing lens, so that we shall call them the focusing fields.

The dispersing field has no focusing action as shown in Eq.(2-23). Therefore the locations of the source and its image relative to the divided fields will not change. But the dispersion is given by

$$D_k = \left(\frac{a}{\partial \epsilon_r^2} \cdot \frac{1}{f_1} + \frac{a}{\partial \epsilon_r^2} \cdot \frac{1}{f_3} + \Phi_2 \right) f_3 \delta' \quad (2-30)$$

Comparing Eqs.(2-28) and (2-30), it is seen that the dispersion increases by $\Phi_2 f_3 \delta'$ in the latter case. Since the magnification does not change, the resolving power of the analyzer will increase by $\Phi_2 f_1 / s$.

If f_1 and f_3 are very large, both dispersion and

resolving power increase very much compared with the ordinary case. For example, if the separated fields are homogeneous magnetic fields ($\mathcal{E}_r^2 = 1$) with $\Phi_1 = \Phi_3 = 30^\circ$, and the inserted field is a magnetic dispersing field with $\Phi_2 = 180^\circ$, then an about fourfold increase in both dispersion and resolution is expected. Nevertheless, the total size of the whole apparatus will not become so large, because the radius of the dispersing field can be kept much smaller than the radius of the focusing field, for the dispersing action does not depend on its radius. Moreover, it is not necessary that the two focusing fields have the same radius a and the same constant \mathcal{E}_r . If the first field has a_1 and \mathcal{E}_{r1} , and the second has a_3 and \mathcal{E}_{r3} , then the dispersion and the resolving power are given as follows:

$$D_h = \left(\frac{a_1}{\mathcal{E}_{r1}^2} \cdot \frac{1}{f_1} + \frac{a_3}{\mathcal{E}_{r3}^2} \cdot \frac{1}{f_3} + \Phi_2 \right) f_3 \delta' \quad (2-31)$$

$$R_h = \left(\frac{a_1}{\mathcal{E}_{r1}^2} \cdot \frac{1}{f_1} + \frac{a_3}{\mathcal{E}_{r3}^2} \cdot \frac{1}{f_3} + \Phi_2 \right) \frac{f_1}{s} \quad (2-32)$$

2.3. Design

In order to get high resolving power for a mass spectrometer, the apparatus must be a double focusing one with electric and magnetic fields. The dispersion with respect to energy will be obtained by the similar combination of three electric fields, that is the electric dispersing field together with two electric focusing fields. If an intermediate image is formed in the region between the electric and magnetic fields, there must be at least three electric and three magnetic fields. However, if the parallel beam goes from the electric field to the magnetic field as in the case of Mattauch-Herzog type

double focusing machine, two focusing fields, i.e. the electric second focusing field and the magnetic first focusing field, may be cut down and the number of the fields reduces from 6 to 4. A toroidal electric field may be used instead of two electric fields, then the apparatus has only three fields, the electric toroidal, the magnetic dispersing and the magnetic focusing fields. The deflection in the electric field and that in the magnetic field should be in opposite directions. For the second focusing fields, a homogeneous magnetic field is preferable for technical reasons.

In this arrangement of the three fields, the double focusing condition in the first order approximation is given by

$$(2/\partial e_{re}) \sin \partial e_{re} \Phi_e = \sin \Phi_{m_3} + \Phi_{m_2} \quad (2-33)$$

where suffices e and m indicate electric and magnetic fields respectively. When this double focusing condition is satisfied, the mass dispersion at the image point is given by

$$D_m = \frac{1}{2} (a_{m_3} + f_{m_3} \Phi_{m_2}) \gamma \quad (2-34)$$

and the resolving power by

$$R = a_e / (\partial e_{re}^2 s) \quad (2-35)$$

Though the r^{-1} magnetic field has no lens action upon the motion of the ions in the r-direction, it has a focusing effect on the motion in the z-direction, because $\partial e_z = 1$. In order to increase the mass dispersion, it is desirable to extend the deflecting angle Φ_{m_2} as large as possible. Whereas the angle was chosen to be $\Phi_{m_2} = 198.1^\circ = 3.457$ by the consideration of the focusing action in z-direction.

The values of Φ_{m_3} and $\partial e_{re} \Phi_e$ were established to be 30°

in order to make the focal lengths large. Then, α_{re} is calculated to be 0.2527 by the double focusing condition (2-33). Since $\alpha_{re} \Phi_e = 30^\circ$, Φ_e becomes 118.7° . The radii of three fields were selected to be $a_e = 30$ cm, $a_{m2} = 22$ cm and $a_{m3} = 120$ cm by the speculation of the sizes, the weights and machining difficulties of the electrodes and magnets. The distance between two successive fields may be chosen arbitrarily, and the following values were adopted for practical convenience in the design of a vacuum chamber: $\Delta_1 = 22$ cm and $\Delta_2 = 24$ cm.

The source and the image are located at the foci of the focusing fields. Therefore, the distance between the source and the first field, ℓ' , and that between the image and the third field, ℓ'' , are calculated by Eq.(2-19) to be $\ell' = 205.6$ cm and $\ell'' = 207.8$ cm.

The schematic diagram of the ion path is shown in Fig.3. The image point for the z-directional focusing is located at $\ell_z'' = 430$ cm in this arrangement. The reason for locating this point so far away the r-directional image point is to prevent a decrease in resolution caused by the ion beam outside the median plane. The mass dispersion perpendicular to the ion beam is calculated to be 475 γ cm and the magnification of the image to be 1.01. If the width of the objective slit is taken to be 0.005 mm, then a maximum resolution of 940 000 may be expected.

2.4. Second order consideration

The second order ion trajectories should be calculated in order to estimate the image defect. The ion path behind

the field may be expressed in the second order approximation by the following equation.²⁰

$$\begin{aligned}
 y' = & a(D_{11}\alpha_r' + D_{21}\beta + D_{41}\rho_1 + D_{11}\alpha_r'^2 + D_{22}\beta^2 + D_{33}\alpha_z'^2 \\
 & + D_{44}\rho_1^2 + D_{55}\xi_1^2 + D_{12}\alpha_r'\beta + D_{14}\alpha_r'\rho_1 + D_{24}\rho_1\beta + D_{35}\alpha_z'\xi_1) \\
 & + x''(E_{11}\alpha_r' + E_{21}\beta + E_{41}\rho_1 + E_{11}\alpha_r'^2 + E_{22}\beta^2 + E_{33}\alpha_z'^2 \\
 & + E_{44}\rho_1^2 + E_{55}\xi_1^2 + E_{12}\alpha_r'\beta + E_{14}\alpha_r'\rho_1 + E_{24}\rho_1\beta + E_{35}\alpha_z'\xi_1)
 \end{aligned}
 \quad (2-36)$$

where α_r' and α_z' are initial angular divergences in r- and z- direction. All the D_{ij} and E_{ij} in the equation have been calculated for the toroidal electric field, for the homogeneous and the dispersing magnetic fields. The results are listed in Appendix.

The second order image width at the position of the final focus can be calculated by combining the above three results. The expression for negligibly small slit width has the form:

$$y_B = a_{m3} (B_{11}\alpha_r'^2 + B_{12}\alpha_r'\beta + B_{22}\beta^2 + B_{33}\alpha_z'^2) \quad (2-37)$$

where α_r and α_z are radial and axial angles of divergence of the ion beam on the entrance side. The coefficients of the second order aberration, B_{11} , B_{12} , B_{22} are expressed as functions of three parameters R_e' , k' and k'' . R_e' is the derivative of the radius of curvature, R_e , of the equipotential line in the r-z plane of the toroidal electric field, and is given by

$$R_e' = \left(\frac{dR_e}{dr} \right)_{r=a_e, z=0} \quad (2-38)$$

Consequently, it may be possible to make $B_{11} = B_{12} = B_{22} = 0$ by choosing suitable values for R_e' , k' and k'' . In our case,

these values are calculated to be

$$R_e' = 0.237 ,$$

$$a_{m2}/R' = 1.124 ,$$

$$a_{m2}/R'' = -0.178 .$$

The remaining coefficient B_{33} can be made zero if the front faces of the electrodes of the toroidal condenser are made cylindrically curved. The condition for $B_{33} = 0$ is satisfied if we take the value

$$a_e/q' = 3.41 ,$$

where q' is the radius of curvature in the $x'-z$ plane at the entrance of the condenser electrodes.

The inclination of the image curve against the focusing beam is also calculated from the second order consideration. The angle between the direction of the focusing ion beam and the image curve at the double focusing point is calculated to be about 24° for directional focusing and 17° for velocity focusing.

The conditions for the second order focusing are shown in Fig. 3 schematically.

3. Construction of High Resolution Mass Spectrometer

The schematic drawing of the high resolution mass spectrometer is shown in Fig. 4 , and Fig. 5 gives a general view. Following, the important parts of the apparatus and the performance are described briefly.

3.1. Dispersing or r^{-1} magnetic field

The dispersing magnetic field is the most important part of the high resolution mass spectrometer. The mean radius or the radius of the curvature of the central beam is 22 cm and the deflecting angle 198.1° . The magnetic field has r^{-1} character and the cross sectional view is shown in Fig. 6. The pole pieces are made of soft iron with a carbon content of about 0.03%, and have conical pole faces. By means of four distant wedge-shaped pieces of phosphor bronze, the pole gap is adjusted so that the vertices of the circular cones of the upper and the lower pole faces are brought exactly to the same point. The pole gap is 15 mm at the mean radius. In order to adjust the pole gap, there is an air gap of 0.5 mm between the upper pole piece and the yoke. Before installation of the analyzer tube, r -dependence of the field was examined. The result is satisfactory as shown in Fig. 7. There are four exciting coils having 12,100 turns each, wound with 0.45 mm ϕ copper wire. The total weight of the magnet is about 400 kg. The electric current to the coils is feeded from the power supply which consists of the rectifiers, the voltage stabilizers and the current stabilizers with the feedback loop. The stability of the power supply is about $1/2 \times 10^{-6}$. The block diagram is shown in Fig. 8.

The analyzer vacuum tube is made of SUS-33 stainless steel in order to reduce magnetizing effects. The monitor electrodes

can be inserted at three different points along the iron path to know where the actual beam travels.

To terminate the fringing magnetic fields, the Herzog iron shield are attached near the entry and the exit of the magnet pole. The location of them and the measured field distribution are shown in Fig. 9. From this distribution curve, the effective field boundary is estimated to be 5.5 mm outside of the pole edge. This agrees well with the expected value given by Herzog. Boundaries of the pole pieces and the Herzog iron shields are curved so that the radii of the curvature of the respective effective boundaries are expected to have the desired values:

$$k' = 195.5 \text{ mm} , \quad k'' = -1 \text{ 237 mm} .$$

3.2. Energy selector

The energy selector consists of the toroidal condenser, the auxiliary electrodes, the α - and β - defining slits, two beam monitors which determine the vertical location of the beam, and the vacuum chamber which encloses these assemblies. All of these components are made of SUS-27 or 18-8 stainless steel except for some insulators. According to the design calculation, the toroidal electric field should have the following parameters:

$$\Phi_e = 118.7^\circ, \quad \partial e_e = 0.252 \text{ 7} , \quad a_e = 30 \text{ cm}$$

$$R_e' = 0.237 \quad a_e / q' = 3.41$$

The dimensions of the condenser electrodes which produce such a field are calculated by means of the method given by H.Liebl and H.Ewald.²² The dimensions of electrodes actually made were measured

with an accuracy of about 0.1 mm. They are:

$$r_a = 309.1 \text{ mm}, \quad r_b = 290.5 \text{ mm},$$

$$R_a = 157.1 \text{ mm}, \quad R_b = 152.7 \text{ mm},$$

where the notations are those used by H.Liebl and H.Ewald. Under these conditions, the field between the electrodes is estimated to have the desired value within an accuracy of 0.2%. The cross section is shown in Fig. 10.

The Herzog end plates are used at the entry and the exit of the toroidal condenser, the effective field boundaries being supposed to be at the ends of the electrodes.²³ At the entry, the face of the electrodes and the Herzog end plate are cylindrically curved, the value of q' being 88 mm.

The auxiliary electrodes are placed above and below the gap of the toroidal electrodes. By applying suitable potentials to them, the field shape near the center may be finely adjusted.

The α - and β - defining slits are placed about 3 cm outside the Herzog end plates. The lateral position and the width of the slit can be adjusted from the outside of the vacuum chamber by means of the micrometer screw heads. Fig.11 shows one of these slits.

3.3. Focusing magnet

The third field is the focusing magnetic field. The focusing magnet is a 30° sector type magnet which yields the uniform or homogeneous magnetic field. The mean radius is 120 cm and the pole gap 15 mm. The Herzog iron shields, similar to these of the

dispersing field, are attached to the entry and the exit of the field. Two exciting coils are used having 12 330 turns each. The total weight of the focusing magnet is about 540 kg. The power supply has the same construction as before.

3.4 Ion source

Ions, formed in a metal housing kept at high voltage, are extracted through an orifice of 2 mm ϕ and accelerated. Then, they are focused on the objective slit by means of the cylindrical Einzel lens system. The lens system consists of three cylindrical electrodes made of aluminum, the first electrode is grounded and accelerates the ions, the second has a suitable potential and decelerates the ions, and the third is grounded and again accelerates the ions. The focal length of the triplet lens system is controlled by changing the potential of the second electrode. The direction of the collimated ion beam can be adjusted mechanically. In a preliminary test, thermal potassium ions from a hot tungsten ribbon were accelerated to about 15 keV. The total current of 1 μ A is easily obtained. The high tension was regulated with a stability of less than 1/2 000 by means of the series regulator tube 5T31 with negative feedback loop.

3.5. Objective slit system

The objective slit is made out of two stainless steel plates of 0.5 mm thickness which are fixed on the rotatable slit holder. The gap of the steel plates is about 0.05 mm. The objective slit width can be adjusted from 0.05 mm to zero by rotating it around the vertical axis at the center of the slit. The vertical location of the slit can be adjusted and, if necessary, the slit is extruded

from the ion path. The horizontal location of the slit is also adjustable. The whole slit system with the vacuum envelope can be moved along the direction perpendicular to the ion path by the screw. The slit position along the ion path is also adjustable.

In front of the objective slit, there is a horizontal slit of 0.5 mm width, the vertical position of which is also adjustable. A mechanical shutter for the ion beam is inserted between the electrostatic lens system and the horizontal slit. A fluorescent substance is coated on the shutter plate, so that we can observe the spot of ions visually through the window. The shutter has another role, it collects the total ions out of the ion source, and we can measure the total ion current to adjust the operational parameters of the ion source.

3.6. Detector

To detect the analyzed ion beam, Ilford Q2 photographic plates were used during the period of the preliminary test. The size of the plate is $45 \times 150 \text{ mm}^2$. The plate holder can be shifted vertically for taking 5~10 series of mass spectra. A detecting slit is placed at the top of the plate holder, and behind the slit a Faraday cage is installed. By setting the detecting slit into the beam plane, the mass spectrum can be detected electrically. The angle between the direction of the beam and the photographic plate is adjustable.

3.7. Vacuum system.

The vacuum envelopes are made of stainless steel, and o-ring gaskets made of viton are used for vacuum seal. Two isolation

valves are installed, one is inserted between the objective slit and the energy selector and the other the focusing magnet and the detector or camera chamber. Therefore we can evacuate independently three portions, the ion source, the analyzer portion and the camera chamber. Three 6 inch oil diffusion pumps are connected to the analyzer portion and one 2.5 inch oil diffusion pump is used as a booster. To prevent the oil back diffusion, a liquid nitrogen trap is attached to each 6 inch pump. The camera chamber has a 6 inch oil diffusion pump with a liquid nitrogen trap and a booster. The ion source and slit system is evacuated by two 3 inch oil diffusion pumps with liquid nitrogen traps and the arrangement of them achieves differential pumping.

The vacuum for the mass spectrometer should be not only as high as possible but also as oil-free as possible. It is supposed that if oil molecules adsorbed to the slit system form insulating layers, then the surfaces of the slit may have extraordinary potentials by the ion bombardment and ions which pass through such a slit may not focus on the detector. When the mass lines on the photographic plate become not so fine as usual, then the objective, α - and β - defining slits must be extracted, lapped and cleaned up.

3.8. Alignment of the apparatus

The toroidal condenser, the dispersing and the focusing magnets are installed on a concrete block. The relative positions of them were adjusted as follows. First, the vertical positions of three fields were adjusted that their median planes lie in the same horizontal plane by means of a level and a cathetometer. Next,

the calculated positions of every necessary point in the median plane were plotted accurately on a aluminum sheet and small holes were bored. Then, the sheet was supported horizontally above the condenser and the magnets. The horizontal positions of three fields were adjusted that the marked points of the fields coincide with the corresponding points indicated by the plumbs hung through the holes of the aluminum sheet. It is supposed that the errors of the setting do not exceed 0.2 mm. The ion source and the slit system are placed on a separated concrete block. The distance between the condenser and the slit system is measured by a 2 m stainless steel rule. The camera chamber is set in the similar way.

3.9. Reduction of stray magnetic field

The high resolution mass spectrometer has two magnets, and the location of the condenser is very close to the focusing magnet. As it is postulated that there is no magnetic field except for the dispersing and the focusing fields, it is very important to reduce the stray magnetic field as much as possible in order to realize a good focusing condition. The distribution of the stray field along the ion path was measured after setting two magnets at the calculated position. During these measurements, the field strength of the dispersing magnetic field was kept at 4 090 gauss and that of the focusing field at 750 gauss. These field strengths are nearly the same as under the operating conditions.

The stray field distribution toward and in the electric field is shown in Fig.12 . Curve 1 shows the case with no magnetic shielding except for the Herzog iron shield, where a considerable amount of the stray field is found. When the energy selector is

covered with silicon steel sheets, the stray field is reduced as shown by curve 2, but the shielding effect is not yet satisfactory. A considerable improvement is attained by inserting a Permalloy pipe between the energy selector and the Herzog iron shield and by inserting laminated iron sheets between the energy selector and the focusing magnet. The result is shown by curve 3. Under the final condition of the magnetic shielding, the total deflection of the beam due to the stray magnetic field may be estimated to be less than 1/1 000 of the total deflection in the magnetic fields.

4. Artificial Multiplets of ^{39}K

As a preliminary test of the apparatus, ^{39}K thermal ions were accelerated, deflected and detected. The photographic plate detection system was adopted. The purpose of this testing was the adjustment of the machine and the measurement of the dispersion and resolution.

The final results are as follows:

mass dispersion on the plate: 14 mm for 0.1% mass difference,
maximum resolving power attained: 1,200,000.

It should be emphasized that the locations of the objective slit, the fields and the detector were very close to the positions which were indicated by the design calculation.

We describe here the procedures and the conditions under which the above results were obtained.

The ^{39}K thermal ions were accelerated to about 14.5 keV. The vacuum during the operation was estimated to be 1×10^{-6} mm Hg in the energy selector, 4×10^{-6} mm Hg in the dispersing magnetic field and 4×10^{-7} mm Hg at the exit of the focusing magnetic field, as measured by ionization gauges. The potential difference between the electrodes of the toroidal condenser was about 1776 volts and it was grounded at the center. The auxiliary electrodes were grounded during the preliminary tests. The exciting current for the dispersing magnet was finely adjusted so that ion beam passed along the calculated orbit. The beam positions in the dispersing field were measured by three monitor electrodes. The field strength of the focusing magnet was adjusted so that the ion current was detected by the Faraday cage in the camera chamber.

The dispersion of the apparatus was measured by the following procedure. When exposures were made, the potentials applied to

the condenser electrodes and also the accelerating voltages were slightly shifted for each successive exposure while keeping the magnetic fields constant, so that nine spectral lines were photographed in one exposure series. The mass dispersion on the photographic plate may be estimated from the potential values corresponding to respective spectral lines. An example of the spectrum thus obtained is shown in Fig.13. The potential shift between successive exposures is about 1.1 volts and the potential of the center line 1776 volts.

From these values and the distances between spectral lines, the mass dispersion on the photographic plate is estimated to be about 14 mm for 0.1% mass difference. The angle between the photographic plate and the direction of the ion beam is about 21° , so the dispersion agrees well with the calculated value. The resolving power is estimated to be about 500,000 for the sharpest line under the following conditions:

the width of the objective slit, 0.008 mm

the width of the α -defining slit, 0.3 mm, $\alpha_{\max} = 1/10,000$

the width of the β -defining slit, 0.3 mm, $\beta_{\max} = 2.5/10,000$

exposure time, 1 second.

The spectral lines thus obtained were considerably curved as can be seen from Fig.14. The next step is to remove the curving effect. As already mentioned, the monitor electrodes can be inserted at three different points along the ion path in the dispersing magnetic field. A 4 mm x 5 mm slit was attached to the top of the monitor electrode which was placed near the entry of the dispersing field as shown in Fig.14. This slit restricted the ion beam in the dispersing magnetic field. The cause of the curving effect has proved to be a slight magnetization of the slit. If it is

slightly magnetized by a magnetic field of about 5,000 gauss and the magnetic field near the upper and lower ends of the hole is increased by about 50 gauss as compared with that near the center over a region of slit thickness, say about 1 mm, then the difference between the lateral position of the center beam and that of the end beam is estimated to be about 0.16 mm at the image point. This makes the spectral lines considerably curved. Formerly, the slit was made of 18-8 stainless steel (JIS SUS 27) sheet and was slightly magnetized unfortunately. It has been replaced by a non-magnetic material, Mo, and the effect has been removed.

Futher improvements in the sharpness of the spectral lines have been accomplished in the following way. Two origins of broadening spectral lines are found out. One is vibrations due to mechanical pumps and the other hum magnetic fields. In order to reduce the stray magnetic field, a number of iron sheets are placed near the magnets. Small vibrations of these sheets caused by the motion of mechanical pumps disturb magnetic fields considerably. In order to reduce this effect, mechanical pumps have been replaced by sorption pumps during exposure.

A considerable 60 Hz hum magnetic field is found in the laboratory where the high resolution mass spectrometer is installed. Even if there is no 60 Hz component in exciting current, a hum magnetic field of a few milligauss is produced in the pole gap. In order to reduce the hum magnetic field, a negative feedback method is adopted. The output of a pick up coil of 75 turns which is wound around the magnet pole piece is amplified, phase-inverted and supplied to a feedback coil of 5 turns. The hum magnetic field in the pole gap is reduced to about one fourth by this device. Also, the beam duct outside the magnet is covered by

Permalloy sheets 0.2 mm thick.

Fig. 15 shows the spectral lines of artificial doublets thus obtained. The lines are considered to correspond mass numbers 1774, 1775 and 1776 respectively. The distance between lines is about 9 mm and line width is measured to be 12 microns, so that the resolving power is estimated to be about 1,200,000.

5. Modifications and Improvements of the Apparatus

By the preliminary results, it is shown that the high resolution mass spectrometer is suitable to the precise measurements of the atomic masses. In order to measure doublet mass differences, however, it is more suitable to adopt the electronic detection method than the photographic detection, because the mass dispersion of the machine is too large to obtain the doublet lines and reference lines on the same photographic plate. Moreover, the electronic detection system has the merit of making the quick and easy adjustment of the focusing (energy and direction) possible. Therefore, some improvements and modifications have been done as described in the following.

5.1. Electron multiplier detection system

A 15-stage electron multiplier is attached behind the camera chamber. The multiplier is demountable, so that the gain of it is not so high as the sealed-off tube and is about 5×10^4 when the supplied voltage is 1750 volts (Fig.16). The noise pulses are very few and they do not disturb the observations.

In front of the multiplier, there is a detector slit in the camera chamber. It is made of two razor blades which are fixed to make the edges face each other with a very narrow gap, so that very long wedge-shaped slit is formed. The shape of the detector slit thus made is of slender triangle, the base and the height of which are about 50 microns and 25 mm respectively. The vertical position of the assembly can be adjusted from outside of the vacuum chamber. In order to restrict the vertical width of the ion beam, another horizontal slit of 1 mm width is placed in front

of the detector slit, the vertical position of which is adjustable independently. The effective width of the detector slit is, therefore, determined by the 1 mm region of 25 mm length. The effective width can be adjustable to have any desired value between 50 microns to 2 microns by shifting the vertical position of the slit assembly.

The output signal is amplified by a preamplifier and then observed on a cathode ray oscilloscope screen. The preamplifier is placed near the multiplier and the circuit diagram of it is shown in Fig.17 .

5.2. Beam scanner

To observe the mass peaks on the CRT screen, ion beam are scanned by a saw-tooth magnetic field which is produced by a Helmholtz type coil placed between the focusing magnetic field and the camera chamber. The ion beam is scanned about 100 microns at the detector slit from left to right or vice versa. The horizontal signal of the oscilloscope is amplified and feeded to the Helmholtz coil, so that the synchronization holds automatically. The scanning width is reduced to one second or one fourth of the nominal value by the reduction of the exciting coil current. The scanning rate can be varied from DC to 60 Hz. The electrical connection of the beam scanner is shown in Fig.18 .

5.3. Ion pump

A ion pump of 8 l/sec (NEC911-0000) is attached to the analyser tube in the dispersing magnetic field. It is our intention to improve the vacuum problem in the analyser tube. The pressure in the region is supposed to be reduced to about

one tenth. In addition to the improvement during the operation of the machine, it holds the pressure in the analyzer envelope to 2×10^{-5} mm Hg after all the oil diffusion pumps have been shut down.

5.4. The effect of 60 Hz hum magnetic field

As already mentioned, a 60 Hz hum magnetic ^{field} affects the ion beam path. However, the effect is not so clearly demonstrated by the photographic plate detection system, although we are convinced of the effect. The electron multiplier and beam scanner show the effect, if there is no protection against the hum magnetic field, then the ion beam fluctuates to and fro about the detector slit and the mass peak suffers from the amplitude modulation. Fig.19(a) shows how the hum magnetic field modulates the beam intensity at the detector.

The feedback device (Section 4) eliminates the beam modulation but it is not always stable and cause sometimes a spurious oscillation. Therefore, in addition to the device, the 60 Hz current, the amplitude and the phase of which is adjusted so that the hum effect is minimized, is feeded to a 5 turn coil which is wound around the pole piece. As the results, the 60 Hz hum effect is mainly cancelled by the latter method and the feedback device reduced higher harmonics, especially 3-rd harmonics. The peak shape thus improved is shown in Fig.19(b).

5.5. Modification of the ion source.

The thermal ion source, which is used during the preliminary test, is very suitable for several sorts of alkali metals.

However, other types of the source must be needed for general purpose. There are two ion sources, which are both home-made, one is a PIG discharge source and the other is a Nier type source.²⁴

Ions are produced by the PIG type discharge in the former source. To stabilize the discharge and to reduce the pressure in the source as low as possible, a hot cathode is attached. Sample gas of about 20 mmHg is introduced to the source through a capillary. The total ion current is $2 \sim 3 \mu\text{A}$ during the normal operation. The $^{12}\text{C}_3\text{H}_8$ - $^{12}\text{C}^{16}\text{O}_2$ mass difference measurement has done with the PIG discharge source.

The PIG discharge gas source yields considerably large ion currents, but its operation becomes instable under the condition that an furnace is installed in the source to vaporize metals. It is supposed that undesirable outgas causes an instability of the discharge. Therefore, a Nier type electron bombard source is used to measure the mass difference of $^{40}\text{Ca} - ^{40}\text{Ar}$ doublet. Calcium molecules are vaporized in the furnace and they diffuse into the ionization chamber where they are bombarded by 90 eV electrons and ionized. Total ion current is $0.1 \sim 0.3 \mu\text{A}$. The ion sources described here are not invariably satisfactory for general purpose. The improvement of the ion source may be one of the most important problem at present. We believe that the improvement should be done along the line of increasing not only the total ion current but also the brightness of the source.

5.6. Beam emittance²⁵

Now we consider how many ions can enter into the energy selector. If the Coulomb interaction of ions is neglected,

then we can treat ions as the ensemble of the identical and independent particles. In accordance with Liouville's theorem, a volume of the six dimensional phase space which is occupied by the ions under consideration should be conserved for a lossless beam transport system, where the ions are affected by a force which is derived from a scalar potential. When the ions travel horizontally, let the mean direction of the ion path be Z- axis and the vertical line be X- axis. If there is no coupling between the longitudinal and the transverse motions of the ions, the invariant $\beta^2 \gamma^2 V_4$ may be obtained in the four dimensional transverse phase space. Here $V_4(x, y, x', y')$ is the four dimensional volume, $x' = Px/Pz$, $y' = Py/Pz$, β and γ have the usual meaning, i.e. $Pz = m_0 c \beta \gamma$. For an axial symmetric beam, it has been shown that $\beta \gamma A_2$ becomes another invariant, where A_2 is the two dimensional phase space area.

The beam emittance and the ion source brightness are defined to establish further criteria by which to judge the performance of the various ion sources. The normalized two dimensional beam emittance is defined by von Steenberg as follows:

$$\epsilon_2 = \frac{\beta \gamma A_2}{\pi}$$

If the total current of an ion source is denoted by I , the normalized source brightness is defined as :

$$B_4 = \frac{I}{\beta^2 \gamma^2 V_4}$$

which specifies the particles unit time density in four dimensional phase space.

Although the beam emittance has not yet been measured, the

maximum ion current which could enter into the energy selector may be estimated.

The ions are extracted through the 2 mm ϕ orifice of the Wehnelt electrode and accelerated to 15 keV. If it is assumed that accelerating system and the Einzel lens system have no aberration and the maximum kinetic energy of the transverse motion is 0.1 eV, then the phase area at the objective slit is

$$A_2 \approx 2 \times \sqrt{\frac{0.1}{1.5 \times 10^4}} \times 2 \text{ (mm-rad)}$$

$$\approx 10 \text{ (mm-mrad)}$$

On the other hand, if the width of the objective slit is 50 microns or 0.05 mm and that of the α -defining slit is 1 mm, then the acceptance in the y-direction is 25×10^{-3} mm-mrad, similarly if the vertical widths of the objective and α -defining slits are 0.5 mm and 2 mm respectively, then the acceptance in the x-direction is 0.5 mm-mrad. If it is assumed that the ions are distributed uniformly in the phase area, then $(1/400) \times (1/20) = 1/8000$ of the total ions may enter into the energy analyzer.

When the total ion current is 0.15 μ A, the current which enter into the energy selector may not exceed 20 $\mu\mu$ A, while the observed value of the accepted current is about 15 $\mu\mu$ A, 1/10,000 of the total current.

In conclusion the improvement of the Einzel lens system does not so greatly increase the accepted ions, and a hot plasma type ion source, for instance a duoplasmatron, is not suitable for the high resolution mass spectrometer because the large thermal energies of ions enlarge the beam emittance.

6. Preliminary Peak Matching Measurement

6.1. Principle of the peak matching method

We consider two ions which have masses M_1 and M_2 and the same charge e . They have the energies:

$$\frac{P_1^2}{2M_1} + e\phi_1 = eV_{01} \quad (6-1)$$

$$\frac{P_2^2}{2M_2} + e\phi_2 = eV_{02} \quad (6-2)$$

where P_1, P_2 are the magnitude of the momentum, ϕ_1, ϕ_2 are the potentials in arbitrary location and V_{01}, V_{02} are the accelerating voltages. If the condition

$$M_1(V_{01} - \phi_1) = M_2(V_{02} - \phi_2) \quad (6-3)$$

is fulfilled everywhere, then

$$P_1 = P_2 \quad (6-4)$$

The ion trajectory in the static electric and magnetic fields is determined by the expression

$$\delta \int (P + eA_s) ds = 0 \quad (6-5)$$

Therefore, if the magnetic field along the whole ion path is in the same condition for the different ions having mass M_1 and M_2 , and the condition (6-3) is fulfilled everywhere, then the two kinds of ions travel exactly along the same orbit and the two

peaks corresponding to M_1 and M_2 will match on the screen.

In order to fulfill the condition (6-3), all electrostatic potentials, i.e. the accelerating voltage, the energy selector potentials, and so on, should be changed at the same rate. When the vacuum chambers and the slit systems of the whole mass spectrometer are kept at the same potential, say ground potential, the only cause of the potential variation along the ion path may be the potentials applied to the condenser electrodes of the energy selector. Let V_1 and V_2 be the energy selector potentials corresponding to M_1 and M_2 respectively, and the accelerating voltages are exactly proportional to them, that is,

$$V_1/V_2 = V_{01}/V_{02} \quad (6-6)$$

Then, the condition (6-3) is replaced by

$$M_1 V_1 = M_2 V_2 \quad (6-7)$$

It follows that:

$$\frac{\Delta M}{M_1} = \frac{\Delta V}{V_2} \quad (6-8)$$

where $\Delta M = M_2 - M_1$ and $\Delta V = V_1 - V_2$

Therefore the measurement of the mass is reduced to the measurement of the voltage.

Even if there are magnetic fields in the region outside the magnetic pole gap, e.g. a stray magnetic field in the energy selector and the terrestrial magnetic field in the source and

beam ducts, as long as they are static, the peak matching method is applicable as easily seen by Eq.(6-5). Obviously the relativistic correction should be done if necessary.

6.2. Experimental preparation

In the practical application of the peak matching method, the two peaks of mass M_1 and M_2 are observed on the same CRT screen by means of the device described below.

The block diagram of the peak matching circuitry is shown in Fig.20 . Synchronous pulses which are generated by the cathode ray oscilloscope actuate a flip-flop circuit and two sets of reed relays operate. One set of relays causes the deflection voltage applied to the condenser electrodes to switch between two different values. The other set produces a similar change in the ion accelerating voltage, insuring that ions of the proper energy are available. Also saw tooth signals of the CRO are amplified and feeded to the scanning coil. The output of the electron multiplier is amplified and displayed on the CRT screen. The switching technique makes it possible to superimpose the two components of the mass doublet on the oscilloscope screen. Thus on sweeps 1,3,5,7, etc., one observes one component of the mass doublet. On sweeps 2,4,6,8,etc., one observes the other component. The gain of the amplifier is variable separately for the two components, making it possible readily to compare two peaks of different intensity.

The block diagrams of the high voltage switching circuit and the energy selector power supply system are shown in Fig.21 and Fig.22 respectively. The peak matching is achieved by

adjusting R in Fig.22 until coincidence is obtained. Also the circuits of a flip-flop and a switching relay are shown in Fig.23(a) and Fig.23(b) respectively. The wave forms of signals and displayed mass spectra are shown in Fig.24 schematically.

6.3. Energy focusing

It may be difficult that the accelerating voltages V_{01} and V_{02} fulfill the condition (6-6), since the stability of accelerating voltage is not so good and the initial kinetic energies of ions are unknown usually. Fortunately, the high resolution mass spectrometer has the energy focusing character and, if this focusing is sufficiently good, slight change in V_{01} and V_{02} do not affect the final positions of ion beam at the collector slit. Therefore, the adjustment of the energy focusing is very important for the precise determination of mass doublet.

The procedure of the energy focusing adjustment is as follows: We observe only one component of mass doublet on the CRT screen by disconnecting the battery for ΔV from the circuit, and operate the relays which produce a slight change, say about 10 V, in the accelerating voltage. If the energy focusing is good, we observe only one peak, due to coincidence, on the screen, but if the focusing is not good, two peaks are observed at a small distance. The adjustment of the energy focusing can be done by changing the ion orbit in the magnetic fields slightly. Since our mass spectrometer has two magnetic fields, dispersing and focusing, ions which have travelled along different orbits in the magnetic fields can enter the same detecting slit, if the field strengths of two magnetic fields are adjusted adequately. Therefore, observing the oscilloscope pattern, the dispersing

magnetic field is increased and the focusing field is decreased at the same time, or vice versa, until the two peaks coincide. The energy focusing is achieved in the region of the mass number 44 when ions travel about 1 mm outside the calculated trajectory in the dispersing magnetic field.

6.4. Direction focusing

As already mentioned, the energy selector has two auxiliary electrodes which are placed above and below the gap of the condenser electrodes. The focal length of the toroidal condenser may be adjusted by applying suitable potentials to the auxiliary electrodes. The variation of the potentials applied to them causes a slight modification of the field shape in the condenser electrodes and the constant \mathcal{E}_{re} which characterizes the focusing nature of the field will be modified as a result. Fig.25 shows the variation of the calculated image position, ℓ'' , along the optical axis with the variation of the constant \mathcal{E}_{re} . As can be seen in the figure, the directional focusing is much more sensitive than the energy focusing. Therefore we can adjust the direction focus effectively apart from the energy focusing by means of the adjustments of the potentials of the auxiliary electrodes. The methods of the focusing adjustments described above are very favourable features of the apparatus.

6.5. Results

According to Eq.(6-7), the mass difference of a doublet, say $^{12}_6\text{C}_3^{16}\text{O}_2 - ^{12}_6\text{C}_3^{18}\text{O}_2$, is determined by three values, i.e., the higher mass or the lower mass of the doublet, the potential of the energy selector electrode which corresponds to the lower

mass ion or the higher mass ion, and the potential difference

$$\Delta V.$$

The potential difference ΔV is measured by a commercially available potentiometer (YEW P-1A) with a voltage divider (YEW BKP-11L). The latter is calibrated by a Wheatstone bridge (YEW BD-1B). The potential supply of the toroidal condenser has no breeder circuit in order to minimize a load current of batteries. Accordingly, the potentials of the electrodes are very stable as long as temperature of batteries is unchanged, and are scarcely suffered from a external electrostatic disturbance. However, since direct measurements of them are very difficult, the potential difference corresponding to $^{12}\text{C}_3\ ^1\text{H}_8 - ^{12}\text{C}_3\ ^1\text{H}_7$ doublet or one hydrogen mass is measured by the method above mentioned. Then ΔM is given by

$$\Delta M = \frac{M_{\text{CO}_2}}{M_{\text{C}_3\text{H}_7}} \cdot M_{\text{H}} \cdot \frac{\Delta V}{\Delta V_{\text{H}}}$$

where M_{CO_2} , $M_{\text{C}_3\text{H}_7}$, M_{H} express the masses of CO_2^+ , C_3H_7^+ , ^1H , and ΔV_{H} is potential difference corresponding to ^1H .

ΔV and ΔV_{H} are measured with the accuracy of 0.01%, whereas the masses of CO_2^+ , C_3H_7^+ and ^1H are determined with the errors of 100 keV or less, so that a percentage error of ΔM is about 0.01%. If ΔM is 10 mu, then the accuracy of an experiment is of the order of 1 μ u. It is desirable for us to measure as narrower doublets as possible because the accuracy of the voltage measurement is not so good.

The present values are shown in Table 2 together with previous values measured or calculated. The values are grouped

according to the day on which the run was performed. The distribution is shown in Fig.26.

The probable error representing the reproducibility of the results is calculated and is $1.7 \mu u$. When this probable error is combined with the error associated with the voltage measurements, the final probable error is obtained.

The oscilloscope pattern of 50 % mismatched peaks and that of matched peaks are shown in Fig.27. A distance on the CRT screen corresponding to the resolving power of 350,000 is also indicated in the figure.

7. $^{40}\text{Ca} - ^{40}\text{Ar}$ Mass Difference

According to the 1961 and 1964 atomic mass tables, ^{40}Ca and ^{40}Ar have very similar mass values.

	^{40}Ca (μu)	^{40}Ar (μu)	$^{40}\text{Ca} - ^{40}\text{Ar}$ (μu)
1961 ¹	39 962 589.2 \pm 3.7	39 962 383.8 \pm 0.8	205.4 \pm 3.8
1964 ¹⁶	39 962 588.9 \pm 3.5	39 962 384.2 \pm 0.8	204.7 \pm 3.6

Since the mass difference $^{40}\text{Ca} - ^{40}\text{Ar}$ is only 205 μu or 191 keV, a base resolution of, at least, 200,000 is necessary for the direct spectrometric determination. Although a half height resolution of 200,000 may separate two peaks, the precise determination of the mass difference may be impossible. Therefore no attempt of direct measurement has yet been done, and masses of ^{40}Ar and ^{40}Ca have been compared with the hydrocarbon $^{12}\text{C}_3^1\text{H}_4$ respectively. The observed values of $^{12}\text{C}_3^1\text{H}_4 - ^{40}\text{Ar}$ and $^{12}\text{C}_3^1\text{H}_4 - ^{40}\text{Ca}$ are:

	$^{12}\text{C}_3^1\text{H}_4 - ^{40}\text{Ar}$ (μu)	$^{12}\text{C}_3^1\text{H}_4 - ^{40}\text{Ca}$ (μu)
K.S.Quisenberry et al. ⁸	68 912.5 \pm 1.3	
C.F.Giese et al. ²⁶	68 912.7 \pm 1.1	68 712.3 \pm 1.5
L.G.Smith ²⁷	68 917.5 \pm 0.38	
Adjusted value ²⁸	68 916.5 \pm 0.7	68 711.9 \pm 3.5

Mattauch et al. adjusted these measured values to prepare the mass table by means of the least squares adjustment. The last values in the above table are thus obtained.

The direct measurement of the $^{40}\text{Ca} - ^{40}\text{Ar}$ mass difference is considered to be very valuable. It will check the reliability of the previous mass values measured and those adjusted in the mass table. It demonstrates also how large resolving power the apparatus has. This work has been done with our high resolution mass spectrometer. The mass difference of $^{40}\text{Ca} - ^{40}\text{Ar}$ obtained in this work is given in the following together with those calculated from the above table.

Present value	$194.3 \pm 3.5 \mu u$
C.F.Giese et al. ²⁶	$200.4 \pm 1.9 \mu u$
²⁸	
Adjusted value	$204.7 \pm 3.6 \mu u$

It is seen that our present value is about $10 \mu u$ smaller than that of the mass table. Fig.2(a) shows the oscilloscope pattern when ΔV in Eq.(6-8) is set at the value corresponding to mass difference $205 \mu u$, and Fig.2(b) shows the matched pattern. The peaks in Fig.2(a) are clearly mismatched. The resolving power in this experiment is estimated to be about 700,000 at one-half the maximum intensity. Therefore it is supposed that the adjusted value of Mattauch et al. is somewhat too large.

The method of the measurement is similar to that described in Section 6 except for the voltage measurement. Instead of the potentiometer, a DC differential voltmeter (Hewlett Packard, Model 740B) is used. The accuracy of voltage measurement is 0.005% and the input impedance is greater than 10^{10} ohms on all range above 10 mV, therefore the errors associated with the voltage measurements is much less than the statistical ones for $^{40}\text{Ca} - ^{40}\text{Ar}$

mass difference measurement. Not only ΔV but also the voltage of the battery V are measured by the DC differential voltmeter.

The measured values of each run are shown in Table 3 and in Fig. 29. The probable error representing the reproducibility of the results is very small and only $\pm 0.45 \mu u$, however, the error associated with the visual observation may be examined additionally. Although the latter is supposed to be less than $1/20$ of the peak width at half-height, it may be rather systematic than random. This error is estimated to be $3 \mu u$, so that the quoted error should be the sum of the two errors, i.e. $\pm 3.5 \mu u$.

The PIG discharge ion source was used on June 30 and July 3, after that it was replaced by the Nier type ion source. There is no appreciable discrepancy between the runs before and after the replacement. Also it has been proved that scanning direction do not affect the measured values.

According to Weissäcker and Bethe's semi-empirical mass formula, the mass difference of $^{40}_{40}\text{Ca}$ and $^{40}_{40}\text{Ar}$ can be estimated approximately. Since $^{40}_{40}\text{Ca}$ and $^{40}_{40}\text{Ar}$ are both even-even nuclei, the mass difference or total energy difference at ground state consists of the differences of the masses of a proton and a neutron, of the Coulomb interaction and of the symmetry energy, and do not depend on the pairing energy. The mass difference is calculated to be about 3.8 MeV and considerably larger than the observed value. Since $^{40}_{40}\text{Ca}$ is one of the most stable nuclei with closed shells of 20 protons and 20 neutrons, the rest mass of $^{40}_{40}\text{Ca}$ may be reduced considerably.

8. Concluding Remarks

A high resolution mass spectrometer was designed and constructed. It installs a r^{-1} type magnetic dispersing field with a toroidal electric field and a homogeneous magnetic field. The resolving power of this apparatus is calculated to be $475/s$, where s is the objective slit width in cm, and the highest value obtained to date is 1,200,000. The new principle of the high resolution mass spectrometer has been verified experimentally. The focusing nature is considerably good and it seems that the second order ion optical calculation with the sharp cut boundary approximation is satisfactory at least so far as experimental conditions concern.

Two types of the detection system and three different ion sources are examined. The photographic plate method can attain the highest resolution²⁹, whereas the peak matching method is convenient to adjust the apparatus, to shorten the measuring time and to simplify the calibration problem. Among three ion sources, i.e. the thermal ion source, the PIG discharge source and the Nier type electron bombard source, the Nier type source is most favourable in general purposes.

The observed mass difference of $^{12}_3\text{C} \text{ } ^1_1\text{H} - ^{12}_{16}\text{C} \text{ } ^0_2\text{O}$ doublet agrees well with previous works and with the value calculated from the 1964 mass table within the error. The measured mass difference of $^{40}_{40}\text{Ca} - ^{40}_{40}\text{Ar}$ doublet, the direct mass comparison of which has not yet been done before, is $194.3 \pm 3.5 \mu\text{u}$. This is somewhat smaller than the previous values calculated. As the values previously reported are manipulated from the indirect measurements, i.e. the comparison to a hydrocarbon, it seems that they are too large.

Although the average of runs performed on a day has a small deviation, it differs appreciably day by day. One of the causes of the discrepancy is supposed to be the situation that it is very difficult to know whether the two peaks are matched precisely, especially for low intensity of ^{40}Ca ions. A 400 channel pulse height analyzer is hoped to resolve the problem. The other causes are a 60 Hz hum magnetic field of power lines and mechanical vibrations associated with rotary pumps, an air conditioner etc. in the room. One of the grounds for attributing the discrepancy to above causes is that the condition for cancellation of a hum differs day after day. Not only the apparatus but also the circumstances must be excellent for such a precise mass measurement.

Acknowledgements.

The author would like to express his sincere appreciation to Professor Hisashi Matsuda, under whose guidance the work was conducted and completed. He wishes to express gratitude to Professor Koreichi Ogata for encouragement and enlightening discussions. He is grateful to Mr. Masao Nojiri who played important part in construction and adjustments of the apparatus, to Mr. Takekiyo Matsuo who performed measurements and prepared different types of ion source, and Mr. Yoshio Kuroda who contributed to the early stage of the work. He would like to thank Professors Tokunosuke Watanabe, Yoshihiro Asano, Toshiyuki Nishiyama, Haruo Saito and Sigenobu Sunagawa for incessant encouragement. He is indebted to Mrs. Toshiko Nakamura for numerical calculations.

References

1. F.Everling, L.A.König, J.H.E.Mattauch and A.H.Wapstra,
Nuclear Physics 15 (1960) 342; 18 (1960) 529; 25 (1961)
177; 28 (1961) 1
L.A.König, J.H.E.Mattauch and A.H.Wapstra, Nuclear Physics
31 (1962) 1; 31 (1962) 18
2. K.Ogata and S.Matsumoto, Proc. Intern. Conf. Nuclidic
Masses, Vienna (1963) p.415
3. R.R.Ries, R.A.Damerow and W.H.Johnson, *ibid.*, p.357
4. R.A.Damerow, Ph.D.Thesis, University of Minnesota (1963)
5. L.G.Smith, Phys. Rev. 90 (1953) 324
L.G.Smith and C.C.Damm, Rev. Sci. Instrum. 27 (1956) 638
6. J.L.Benson and W.H.Johnson, Phys. Rev. 141 (1966) 1112
7. K.Ogata and H.Matsuda, Z. Naturforschg. 10 a (1955) 843
8. K.S.Quisenberry, T.T.Scolman and A.O.Nier, Phys.Rev. 102
(1956) 1071
9. C.Stevens, J.Terandy, G.Lobell, J.Wolfe, N.Beyer and R.
Lewis, Proc. Intern. Conf. Nuclidic Masses, Toronto (1960)
p.403
10. N.R.Isenor, R.C.Barber and H.E.Duckworth, *ibid.*, p.439
11. R.C.Barber, R.L.Bishop, L.A.Cambey, H.E.Duckworth, J.D.
Macdougall, W.McLatchie, J.H.Ormrod and P.van Rookhuyzen,
Proc. Intern. Conf. Nuclidic Masses, Vienna (1963) p.393
12. K.T.Bainbridge and P.E.Moreland, *ibid.*, p.460
13. H.Hintenberger, J.H.E.Mattauch, H.Wende, H.Voshage and
W.Müller-Warmuth, Advan. Mass Spectr. 2 (1963) p.180

14. H.Ewald, E.Konecny, H.Opower and H.Rösler, *ibid.*, p.189;
Z.Naturforschg. 19 a (1964) 194
15. R.A.Demirkhanov, T.I.Gutkin, V.V.Dorokhov and A.D.Rurenko,
Atomic Energy (USSR) 2 (1956) 21
16. J.H.E.Mattauch, W.Thiele and A.H.Wapstra, Nuclear Physics
67 (1965) 1
17. H.Matsuda, Mass Spectroscopy (Japan) 11 (1964) 127
18. H.Matsuda, S.Fukumoto, Y.Kuroda and M.Noziri, Z. Natur-
forschg. 21 a (1966) 25
19. C.A.McDowell, Mass Spectrometry, McGraw-Hill (1963) p.264
20. H.Matsuda, Mass Spectroscopy (Japan) 12 (1964) 47; 12
(1964) 105; 12 (1965) 165; 13 (1965) 59; 13 (1965) 124
21. 伏見康治, 古典力学, 岩波書店 (1964) p.179
22. H.Lieble and H.Ewald, Z. Naturforschg. 14 a, (1959) 842
23. R.Herzog, Phys. Z. 41 (1940) 18
24. C.A.McDowell, Mass Spectrometry, McGraw-Hill (1963) p.69
25. A.van Steenberg, IEEE Trans. on Nuclear Science (June
1965) 746
26. C.F.Giese and J.L.Benson, Phys. Rev. 110 (1958) ⁷¹²~~721~~
27. L.G.Smith, Phys. Rev. 111 (1958) 1606
28. J.H.E.Mattauch, W.Thiele and A.H.Wapstra, Nuclear Physics
67 (1965) 73
29. P.E.Moreland, Ph.D.Thesis, Harvard University (1962)
30. K.S.Quisenberry, C.F.Giese and J.L.Benson, Phys. Rev.
107 (1957) 1664

Appendix

The Coefficients of the Second Order Aberration

The ion path behind the field may be expressed by Eq.(2-36), where α_r , β , ρ , α_z and ξ , show the initial values at the entry of the field, and x'' the distance between the exit boundary and the image. Under the assumption that the field has the effective sharp cut boundaries at the entry and exit, the coefficients of the second order aberration, D_{ij} and E_{ij} in Eq.(2-36), are given as follows.

A.1. The toroidal electric field²⁰

$$D_1 = \frac{1}{\alpha_r} \sin \alpha_r \Phi,$$

$$D_2 = \frac{2}{\alpha_r^2} (1 - \cos \alpha_r \Phi),$$

$$D_4 = \cos \alpha_r \Phi,$$

$$D_{11} = \frac{1}{3\alpha_r^2} \left(1 - \frac{2A}{\alpha_r^2}\right) \cos \alpha_r \Phi + \frac{2}{3\alpha_r^2} \sin^2 \alpha_r \Phi + \frac{A}{3\alpha_r^4} \cos^2 \alpha_r \Phi \\ + \frac{A}{3\alpha_r^4} - \frac{1}{3\alpha_r^2},$$

$$D_{22} = \frac{1}{3\alpha_r^2} \left(3 + \frac{28}{\alpha_r^2} + \frac{16A}{\alpha_r^4}\right) (1 - \cos \alpha_r \Phi) \\ - \frac{2}{\alpha_r} \left(1 + \frac{1}{\alpha_r^2} + \frac{2A}{\alpha_r^4}\right) \Phi \sin \alpha_r \Phi + \frac{4}{3\alpha_r^4} \left(\frac{A}{\alpha_r^2} - 2\right) \sin^2 \alpha_r \Phi,$$

$$D_{33} = \frac{1}{\alpha_r^2} \left(1 - \frac{B}{5\alpha_r^2 - 2}\right) \cos \alpha_r \Phi + \frac{B}{4\alpha_r^2(5\alpha_r^2 - 2)} \cos 2\alpha_r \Phi \\ + \frac{1}{\alpha_r^2} \left(\frac{B}{4\alpha_r^2} - 1\right),$$

$$D_{44} = -\frac{1}{3} \left(1 + \frac{A}{\alpha_r^2}\right) \cos \alpha_r \Phi + \frac{A}{3\alpha_r^2} \sin^2 \alpha_r \Phi \\ + \frac{2}{3} \cos^2 \alpha_r \Phi - \frac{1}{3} \left(1 - \frac{A}{\alpha_r^2}\right),$$

$$D_{35} = \left(\frac{\partial e_z^2}{\partial e_r^2} - \frac{B(3\partial e_z^2 - 2)}{2\partial e_r^2(5\partial e_z^2 - 2)} \right) \cos \partial e_r \Phi - \frac{B}{4(5\partial e_z^2 - 2)} \cos 2\partial e_r \Phi \\ + \frac{1}{\partial e_r^2} \left(\frac{B}{4} - \partial e_z^2 \right) + \frac{a_e}{2q'} \cdot \frac{1}{\partial e_r} \sin \partial e_r \Phi ,$$

$$D_{12} = \frac{1}{\partial e_r} \left(1 + \frac{11}{3\partial e_r^2} + \frac{2A}{3\partial e_r^4} \right) \sin \partial e_r \Phi \\ - \left(1 + \frac{1}{\partial e_r^2} + \frac{2A}{\partial e_r^4} \right) \Phi \cos \partial e_r \Phi - \frac{2}{3\partial e_r^3} \left(2 - \frac{A}{\partial e_r^2} \right) \sin 2\partial e_r \Phi ,$$

$$D_{14} = \frac{1}{3\partial e_r} \left(\frac{2A}{\partial e_r^2} - 1 \right) \sin \partial e_r \Phi + \frac{1}{3\partial e_r} \left(2 - \frac{A}{\partial e_r^2} \right) \sin 2\partial e_r \Phi ,$$

$$D_{24} = \frac{4}{3\partial e_r^2} \left(1 + \frac{A}{\partial e_r^2} \right) \cos \partial e_r \Phi + \left(\frac{1}{\partial e_r} + \partial e_r + \frac{2A}{\partial e_r^3} \right) \Phi \sin \partial e_r \Phi \\ - \frac{4A}{3\partial e_r^4} \sin^2 \partial e_r \Phi - \frac{8}{3\partial e_r^2} \cos^2 \partial e_r \Phi + \frac{4}{3\partial e_r^2} \left(1 - \frac{A}{\partial e_r^2} \right) ,$$

$$D_{35} = \frac{B}{5\partial e_z^2 - 2} \left(\frac{1}{\partial e_r} \sin \partial e_r \Phi - \frac{1}{2\partial e_z} \sin 2\partial e_z \Phi \right) ,$$

$$E_1 = \cos \partial e_r \Phi ,$$

$$E_2 = \frac{2}{\partial e_r} \sin \partial e_r \Phi ,$$

$$E_4 = -\partial e_r \sin \partial e_r \Phi ,$$

$$E_{11} = \frac{1}{3\partial e_r} \left(\frac{2A}{\partial e_r^2} - 1 \right) \left(\sin \partial e_r \Phi - \frac{1}{2} \sin 2\partial e_r \Phi \right) ,$$

$$E_{22} = \frac{1}{\partial e_r} \left(-1 + \frac{10}{3\partial e_r^2} + \frac{4A}{3\partial e_r^4} \right) \sin \partial e_r \Phi \\ - 2 \left(1 + \frac{1}{\partial e_r^2} + \frac{2A}{\partial e_r^4} \right) \Phi \cos \partial e_r \Phi + \frac{2}{3\partial e_r^3} \left(\frac{2A}{\partial e_r^2} - 1 \right) \sin 2\partial e_r \Phi ,$$

$$E_{33} = \frac{1}{\partial r} \left(\frac{B}{5\partial r^2 - 2} - 1 \right) \sin \partial r \Phi - \frac{B}{2\partial r (5\partial r^2 - 2)} \sin 2\partial r \Phi \\ + \frac{a_e}{2q''} \frac{1}{\partial r^2} \sin^2 \partial r \Phi ,$$

$$E_{44} = \frac{1}{3} \left(\partial r + \frac{A}{\partial r} \right) \sin \partial r \Phi + \frac{1}{3} \left(\frac{A}{\partial r^2} - \frac{1}{2} \right) \sin 2\partial r \Phi ,$$

$$E_{55} = \frac{1}{\partial r} \left[\frac{B(3\partial r^2 - 2)}{2(5\partial r^2 - 2)} - \partial r^2 \right] \sin \partial r \Phi + \frac{\partial r B}{2(5\partial r^2 - 2)} \sin 2\partial r \Phi \\ + \frac{a_e}{2q'} \cos \partial r \Phi + \frac{a_e}{2q''} \cos^2 \partial r \Phi ,$$

$$E_{12} = \frac{2}{3\partial r^2} \left(1 - \frac{2A}{\partial r^2} \right) (\cos \partial r \Phi - \cos 2\partial r \Phi) \\ + \left(\partial r + \frac{1}{\partial r} + \frac{2A}{\partial r^3} \right) \Phi \sin \partial r \Phi ,$$

$$E_{14} = \frac{1}{3} \left(\frac{2A}{\partial r^2} - 1 \right) (\cos \partial r \Phi - \cos 2\partial r \Phi) ,$$

$$E_{24} = \frac{1}{\partial r} \left(\frac{5}{3} + \partial r^2 + \frac{2A}{3\partial r^2} \right) \sin \partial r \Phi + \left(1 + \partial r^2 + \frac{2A}{\partial r^2} \right) \Phi \cos \partial r \Phi ,$$

$$E_{35} = \frac{B}{5\partial r^2 - 2} (\cos \partial r \Phi - \cos 2\partial r \Phi) + \frac{a_e}{q'} \cdot \frac{1}{2\partial r} \sin 2\partial r \Phi ,$$

where

$$A = -(6 + 4l + l_2) ,$$

$$B = -(1 - l - 2l_2) ,$$

$$l = - \left(1 - \frac{a}{R_e} \right) ,$$

$$l_2 = 1 + \frac{a}{R_e} + \frac{1}{2} \left(\frac{a}{R_e} \right)^2 (1 + R_e') ,$$

$$\alpha e_r^2 = 3 + \ell$$

Φ is the deflecting angle and R_e the radius of curvature of the equipotential line $\phi=0$ in r - z plane. R_e' is defined by

$$R_e' = \left(\frac{dR_e}{dr} \right)_{r=a}$$

Since ℓ and ℓ_2 are related to the coefficients of expansion, the electrostatic potential near the median plane is expressed as follows.

$$\begin{aligned} \phi(\rho, \zeta) = -a E_0 \left[\rho + \frac{\ell}{2} \rho^2 - \frac{1}{2} (1+\ell) \zeta^2 + \frac{\ell_2}{2} \rho^3 \right. \\ \left. + \frac{1}{2} (1-\ell-2\ell_2) \rho \zeta^2 \right] \end{aligned}$$

ρ' and ρ'' denote the radii of the curvature of the electrodes in the x' - z plane at the entry and in the x'' - z plane at the exit respectively. The centers of curvature are on the x' and x'' axes, and the case in which ρ' or ρ'' is convex towards the outside is defined as positive.

A.2. The dispersing magnetic field¹⁸

$$\begin{aligned} D_1 &= \Phi, & D_2 &= \frac{1}{2} \Phi^2, & D_4 &= 1, \\ D_{11} &= \frac{1}{4} \Phi^2, & D_{22} &= \frac{1}{12} \Phi^4 - \frac{1}{2} \Phi^2, \\ D_{33} &= -\frac{1}{8} (1 - \cos 2\Phi), & D_{44} &= \frac{1}{2} \frac{a}{R_e} \Phi, \\ D_{55} &= \frac{1}{8} (1 - \cos 2\Phi), & D_{12} &= \frac{1}{3} \Phi^3, & D_{14} &= \Phi, \\ D_{24} &= \frac{1}{2} \Phi^2, & D_{35} &= \frac{1}{4} (2\Phi - \sin 2\Phi), \end{aligned}$$

$$\begin{aligned}
E_1 &= 1, & E_2 &= \Phi, & E_4 &= 0, \\
E_{11} &= \frac{1}{2} \frac{a}{R''} \Phi^2 - \frac{1}{2} \Phi, & E_{22} &= \frac{1}{8} \frac{a}{R''} \Phi^4 - \frac{1}{6} \Phi^3 - \Phi, & E_{33} &= -\frac{1}{4} \sin 2\Phi, \\
E_{44} &= \frac{1}{2} a \left[\frac{1}{R'} + \frac{1}{R''} \right], & E_{55} &= \frac{1}{4} \sin 2\Phi, \\
E_{12} &= \frac{1}{2} \frac{a}{R''} \Phi^3 - \frac{1}{2} \Phi^2, & E_{14} &= \frac{a}{R''} \Phi, & E_{24} &= \frac{1}{2} \frac{a}{R''} \Phi^2, \\
E_{35} &= \frac{1}{2} (1 - \cos 2\Phi),
\end{aligned}$$

where R' and R'' are the radii of curvature of the field boundaries at the entry and exit.

A.3. The homogeneous magnetic field (the case of normal incidence and exit.)²⁰

$$\begin{aligned}
D_1 &= \sin \Phi, & D_2 &= 1 - \cos \Phi, & D_4 &= \cos \Phi, \\
D_{11} &= -\frac{1}{4} + \frac{1}{2} \cos \Phi - \frac{1}{4} \cos 2\Phi, \\
D_{22} &= D_{44} = \frac{1}{4} (\cos 2\Phi - 1), & D_{33} &= D_{55} = 0, \\
D_{12} &= \sin \Phi - \frac{1}{2} \sin 2\Phi, & D_{14} &= 0, \\
D_{24} &= \frac{1}{2} - \frac{1}{2} \cos \Phi, & D_{35} &= 0, \\
E_1 &= \cos \Phi, & E_2 &= \sin \Phi, & E_4 &= -\sin \Phi, \\
E_{11} &= -\frac{1}{2} \sin \Phi, & E_{22} &= -\sin \Phi, & E_{33} &= E_{44} = E_{55} = 0, \\
E_{12} &= E_{14} = 0, & E_{24} &= \sin \Phi, & E_{35} &= 0
\end{aligned}$$

The second order image width at the position of the final focus can be calculated by combining the above three results. When the double focusing condition is fulfilled, the expression for negligibly small slit width has the form of Eq. (2-37).

List of Tables

Table

- 1 Parameters and resolving powers of the present r^{-1} type
and typical ordinary high resolution mass spectrometers.
- 2 The observed values and previous works $^{12}_3C$ 1_8H - $^{12}_{16}C$ 0_2O .
- 3 The measured values of the mass difference $^{40}_{40}Ca$ - $^{40}_{40}Ar$.

List of Figures

Figure

1. Barber's rule.
2. Schematic diagrams which show the principle of the high resolution mass spectrometer with dispersing field.
3. Schematic diagram of the ion path.
4. Schematic drawing of the mass spectrometer.
5. General view of the high resolution mass spectrometer.
6. Cross section of the dispersing magnet.
7. r -dependence of the dispersing field.
8. Block diagram of magnet power supply.
9. Herzog iron shield and fringing field distribution.
10. Cross section of the energy selector.
11. The β -defining slit.
12. Effect of shielding on stray magnetic field.
13. Example of artificial multiplets.
14. Movable slit in the dispersing magnetic field.
15. Example of improved mass spectral lines.
16. The 15-stage electron multiplier.
17. The circuit diagram of the preamplifier.
18. The circuit diagram of the beam scanner.
19. Cancellation of the 60 Hz hum magnetic field.
20. The block diagram of the peak matching circuitry.
21. The block diagram of the high voltage switching circuit.
22. The block diagram of the energy selector power supply.
23. The circuit diagrams of the flip-flop and the driver of reed relay.

Figure

24. Phase relationships in peak matching circuits.
25. $\partial \mathcal{C}_{re}$ -dependence of the image distance.
26. A histogram of 26 values of mass difference $C H - CO$.
3 8 2
27. $C H - CO$ doublet displayed on CRT.
3 8 2 40 40
28. The oscilloscope patterns of $Ca - Ar$ doublet.
40 40
29. A histogram of 26 runs of mass difference $Ca - Ar$.

Table 1 Parameters and resolving powers of the present r^{-1} type and typical ordinary high resolution mass spectrometers

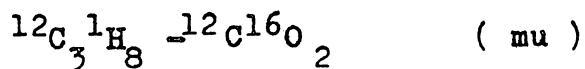
Apparatus	a_e (cm)	Φ_e	a_m (cm)	Φ_m	L (m)	Resolving power	
						Calculated for 1 micron slit	Attained at half- height
Present r^{-1} type	30	118.7°	22* 120**	198.1°* 30°**	6.6	4 750 000	1 200 000 (1965)
K.Ogata and H.Matsuda (Osaka University)	109.3	84°48'	120	60°	9.9	1 640 000	900 000 (1956)
K.T. Bainbridge et al. (Harvard University)	213.36	31°50'	126.75	90°	5	1 067 000	100 000 (1960) 360 000 (1962)
H.Hintenberger et al. (Max Planck-Institute)	542.6	48°26'	100	166°59'	15	2 500 000	60 000 (1961) 200 000 (1963)
A.O.Nier et al. (Minnesota University)	50.31	90°	40.64	60°	3.05	503 000	300 000 (1963)
H.E.Duckworth et al. (MacMaster University)	274	90°	274	180°	15	2 740 000	200 000 (1963)

* dispersing field a_e : radius of the central beam in the energy selector

** focusing field a_m : radius of the central beam in the magnetic field

L : total length of the ion path Φ_e and Φ_m : deflection angles of the electric and magnetic fields

Table 2 The observed values and previous works



	April 25/67	May 16/67	May 17/67
	72. 759 15	72. 791 99	72. 770 90
	72. 786 41	72. 746 74	72. 771 48
	72. 786 41	72. 814 62	72. 770 32
	72. 788 15	72. 765 89	72. 768 61
	72. 780 61	72. 791 99	72. 772 09
	72. 762 05	72. 771 69	72. 777 84
	72. 774 22	72. 772 85	72. 770 35
	72. 775 97		72. 765 57
			72. 763 83
			72. 769 05
			72. 773 66
Mean	72. 776 63	72. 779 40	72. 769 60

Mean of 26 runs : 72. 774 5 $\mu\text{u} \pm 10 \mu\text{u}$

Previous works

K.S.Quisenberry et al. ⁸	72. 763 9	$\mu\text{u} \pm 1.6 \mu\text{u}$
K.S.Quisenberry et al. ³⁰	72. 770 1	$\mu\text{u} \pm 1.6 \mu\text{u}$
L.G.Smith ²⁷	72. 771 9	$\mu\text{u} \pm 0.5 \mu\text{u}$

Calculated from the mass table

1961 ¹	72. 771 9	$\mu\text{u} \pm 0.86 \mu\text{u}$
1964 ¹⁶	72. 771 5	$\mu\text{u} \pm 0.86 \mu\text{u}$

Table 3

The measured values of the mass difference

$$^{40}\text{Ca} - ^{40}\text{Ar} \quad (\mu\text{u})$$

	June 30/67	July 3/67
	194.8	196.6
	198.4	191.0
	196.9	191.0
	204.2	190.4
		189.0
		196.4
		195.0
		195.1
Mean	<hr/> 198.58	<hr/> 193.06
	July 20/67	July 25/67
	192.7	196.2
	189.4	194.8
	193.4	196.9
	191.4	196.1
	195.5	198.3
	190.1	195.5
	191.4	
	192.1	
Mean	<hr/> 192.04	<hr/> 196.30

Mean of 26 runs : 194.34 ± 0.45

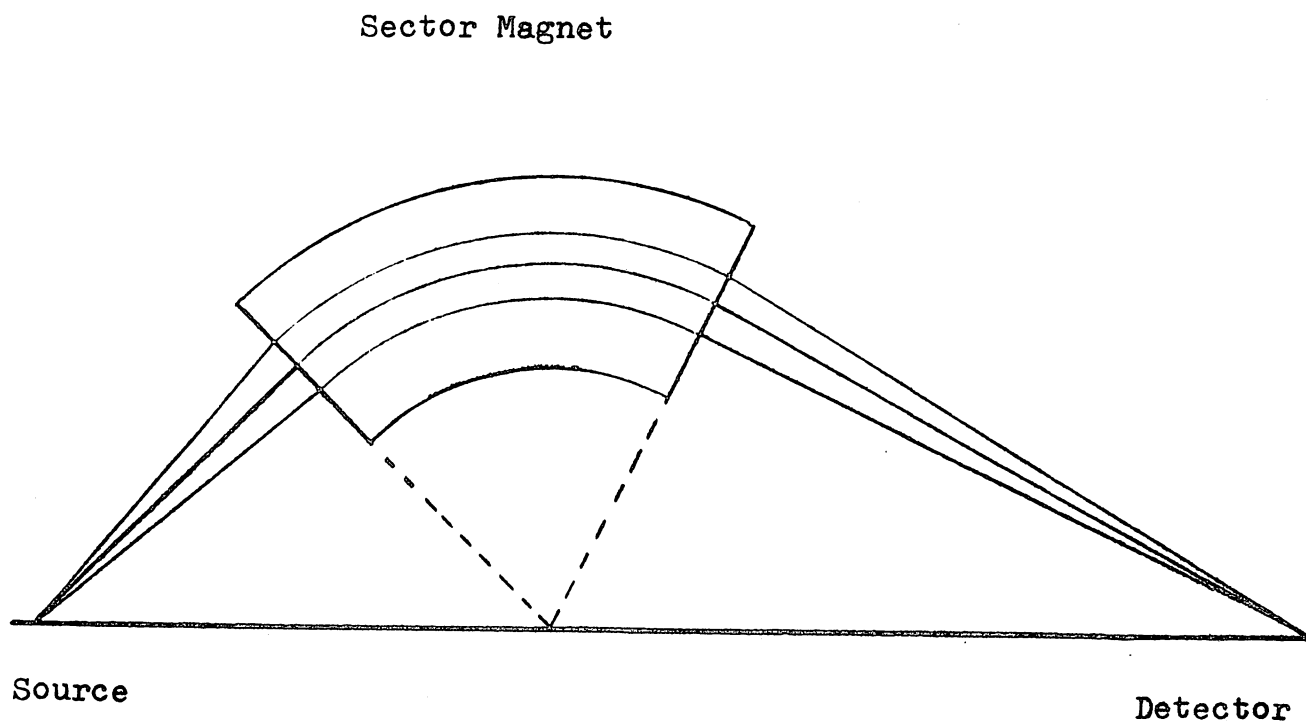
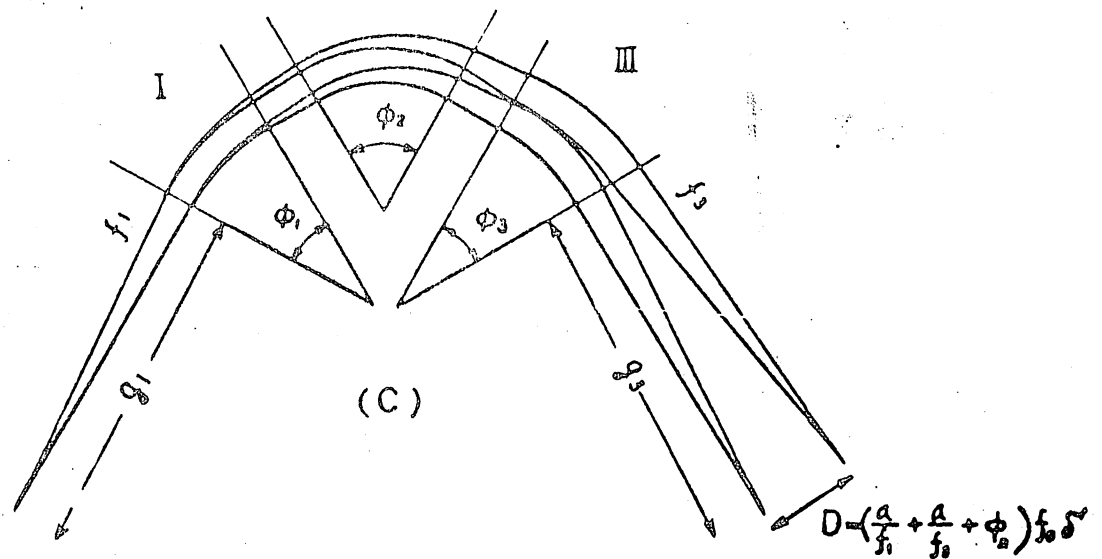
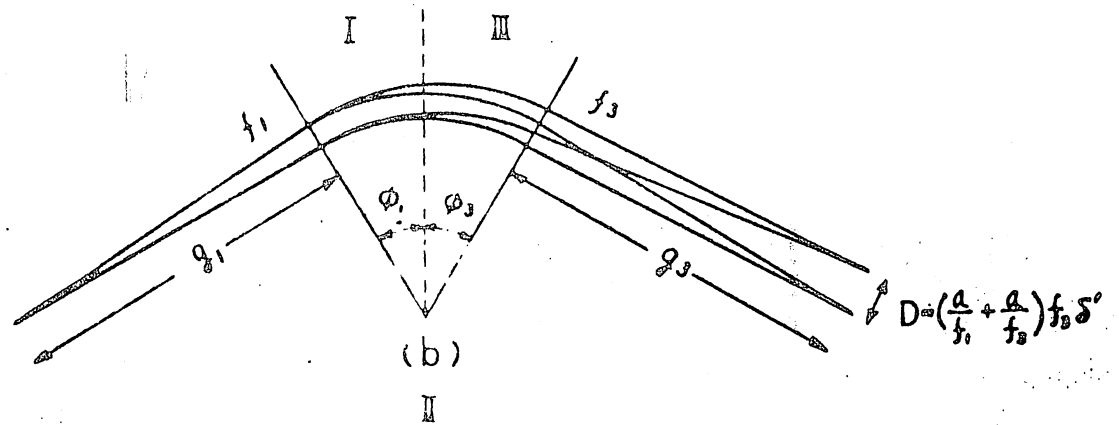
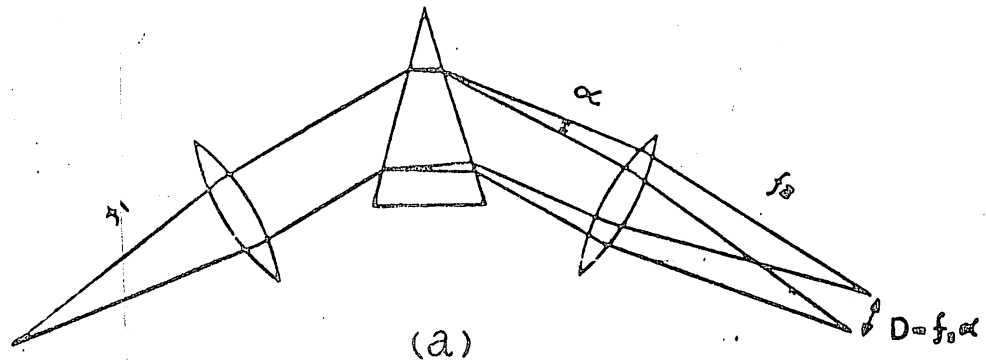


Fig.1. Barber's rule

The ion source, the apex of the field and the image point all lie on one and the same straight line.

Fig.2. Schematic diagrams which show the principle of the high resolution mass spectrometer with dispersing field.



(a) Optical prism spectrograph

(b) Ordinary mass spectrometer

(c) Mass spectrometer with dispersing field

ϕ_e	118.7°	Δ_1	22 cm
a_e	30 cm	Δ_2	24 cm
χ_e	0.2527		
$l'-g_e$	205.6 cm	dR_e/dR_e	0.237
f_e	2374 cm	a_{m2}/k'	1.124
ϕ_{m2}	198.1°	a_{m2}/k'	0.178
a_{m2}	22 cm	a_e/g'	3.41
n	-1		
ϕ_{m3}	30°	l_i	438 cm
a_{m3}	120 cm		
$l'-g_{m2}$	207.8 cm	Dispersion	4757 cm
f_{m3}	240 cm	Magnification	1.01

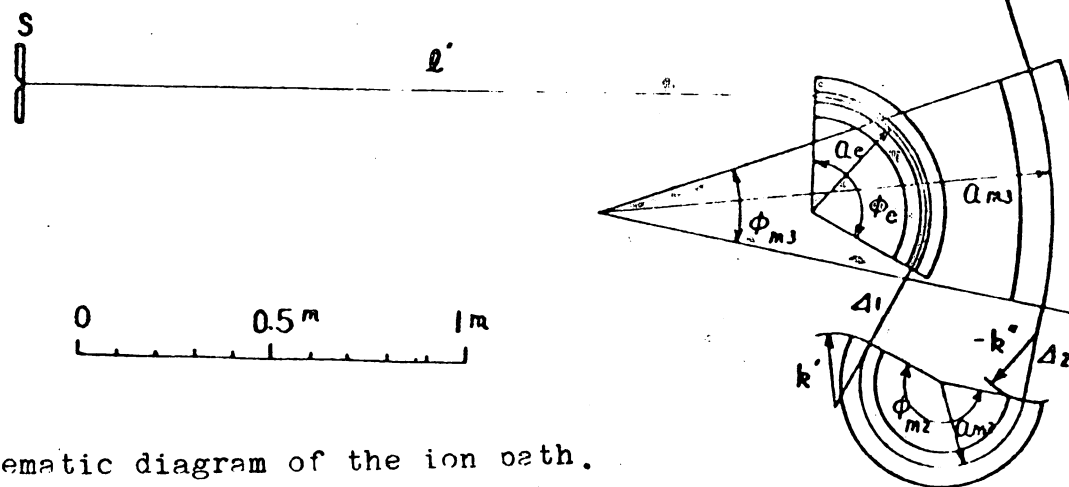


Fig. 3. Schematic diagram of the ion path.

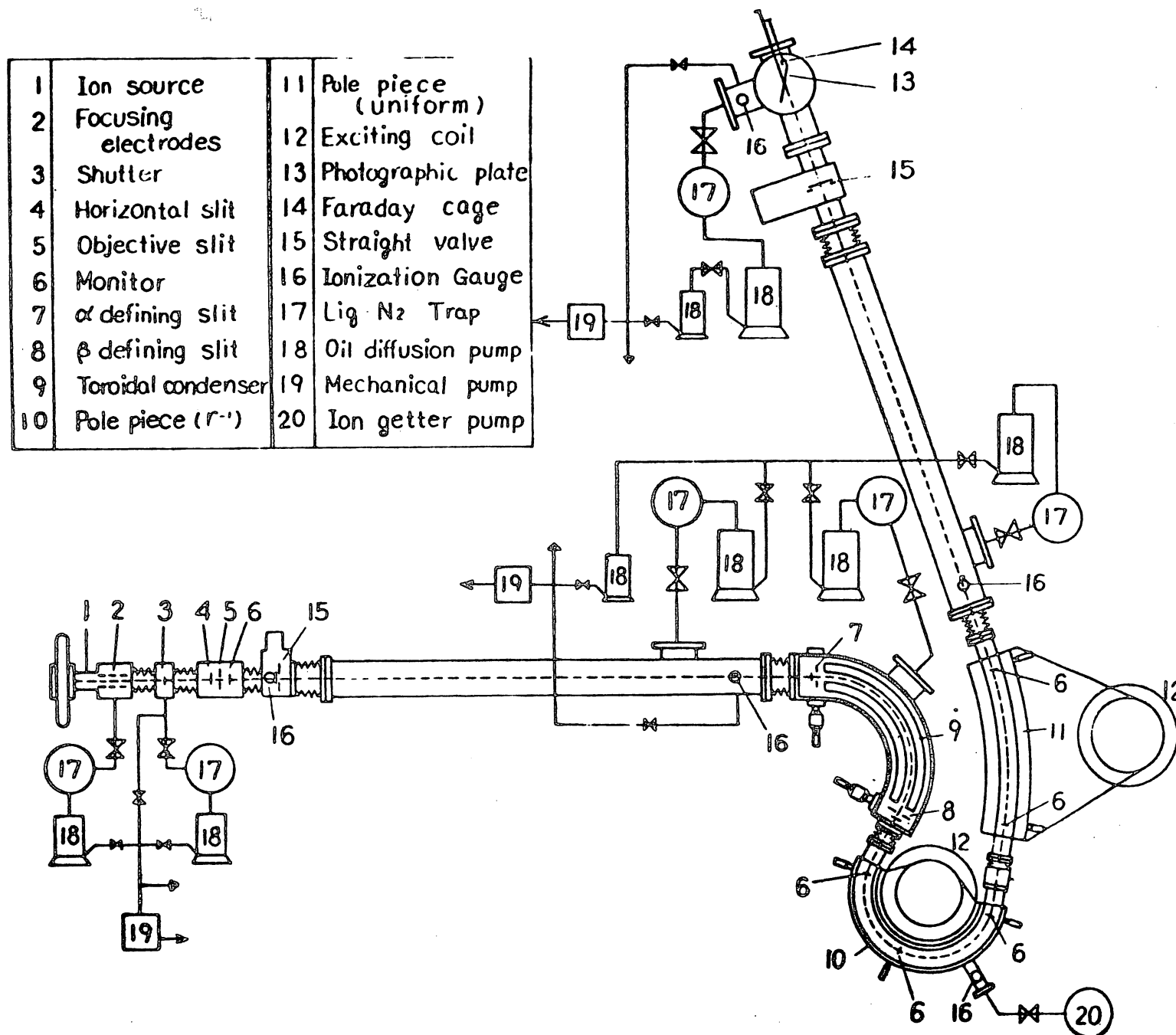


Fig.4. Schematic drawing of the mass spectrometer.

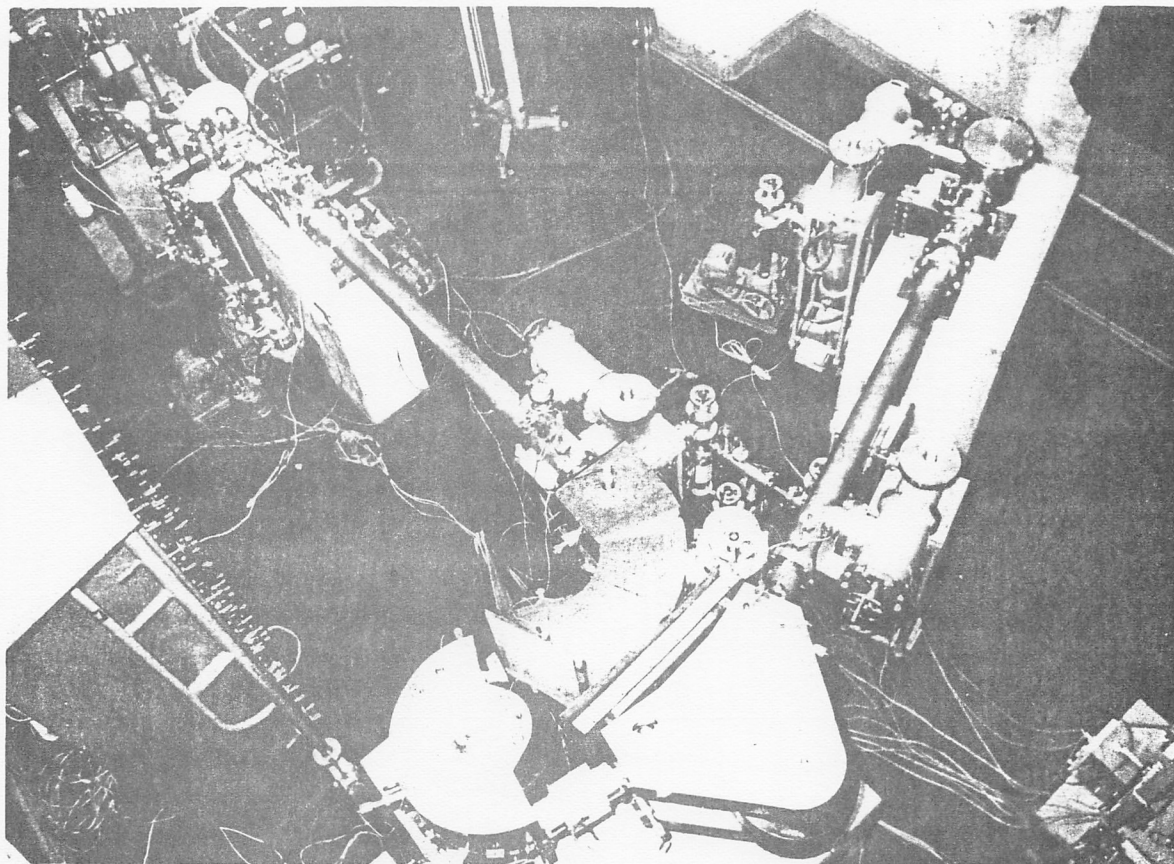


Fig.5. General view of the high resolution mass spectrometer.

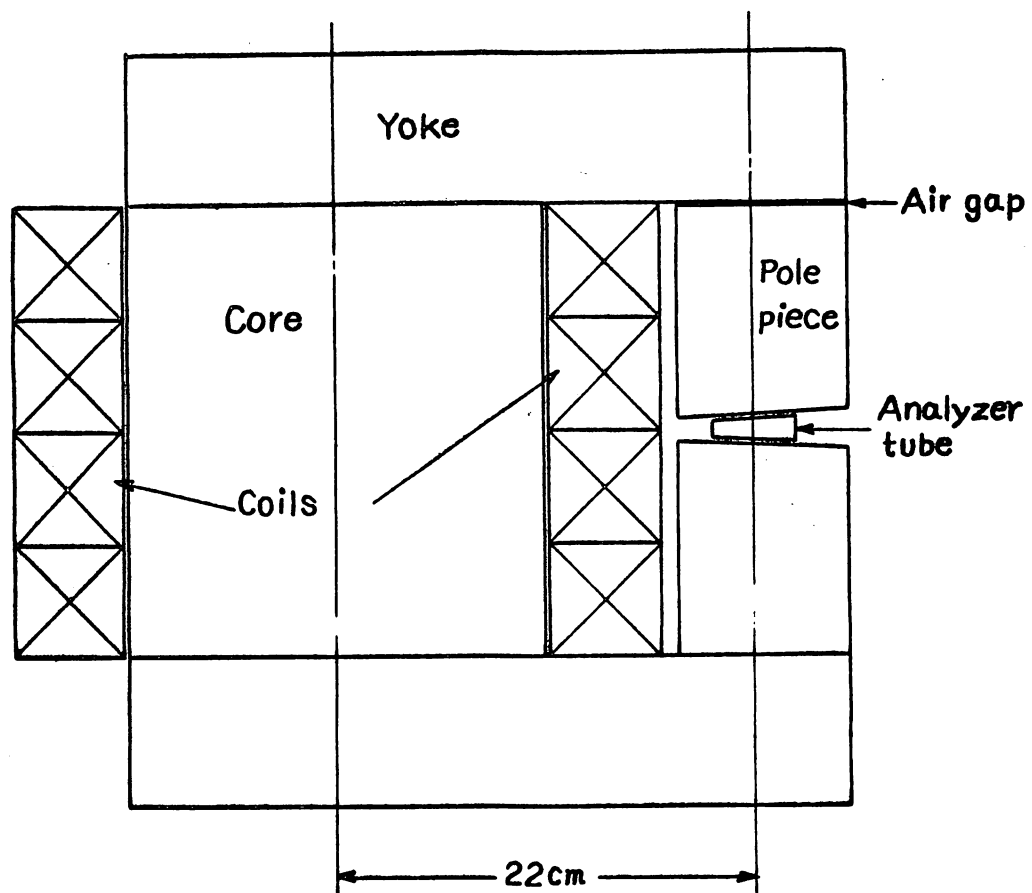
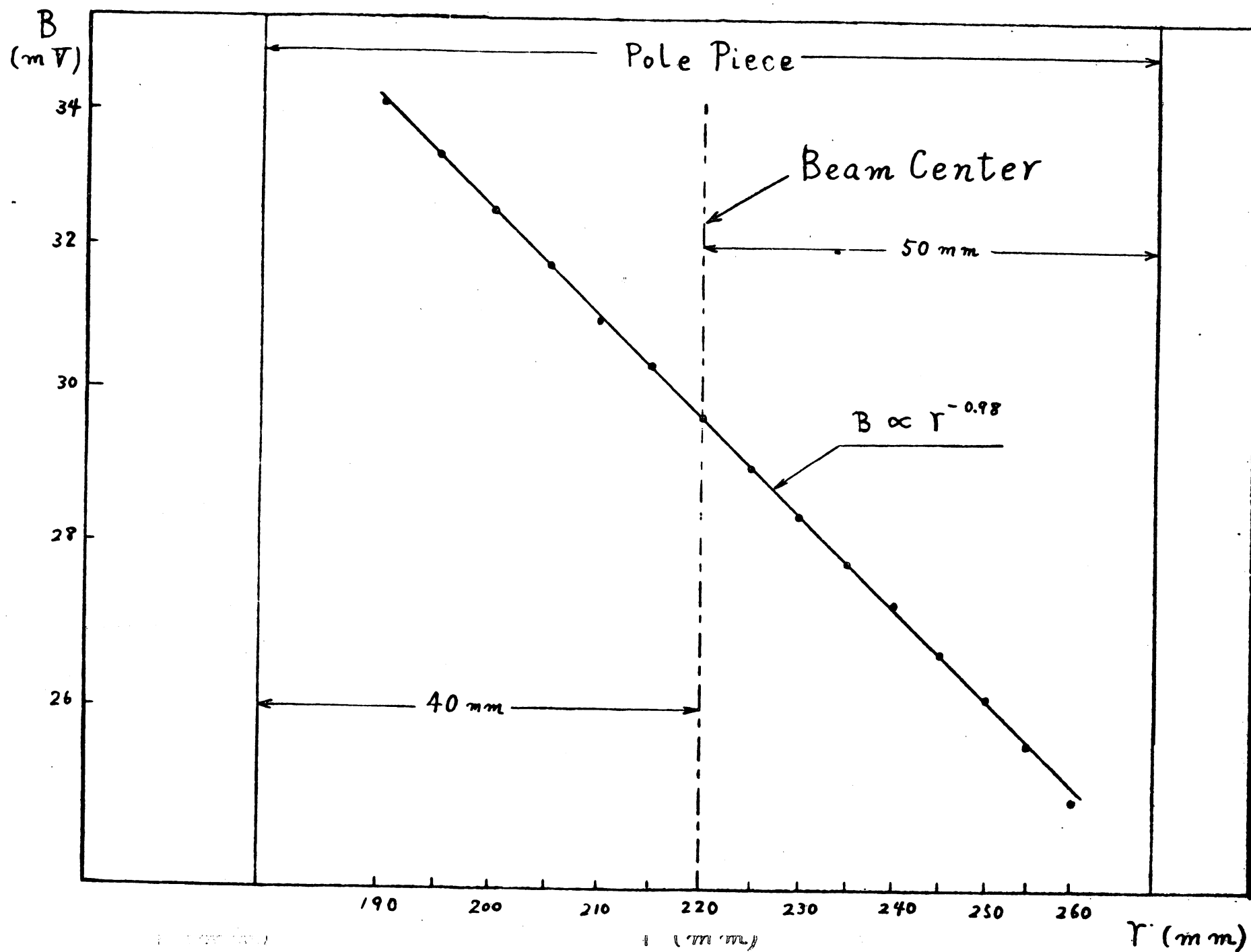


Fig.6. Cross section of the dispersing magnet.

dependence of the dispersing magnetic field. dependence of the dispersing magnetic field. dependence of the dispersing magnetic field.



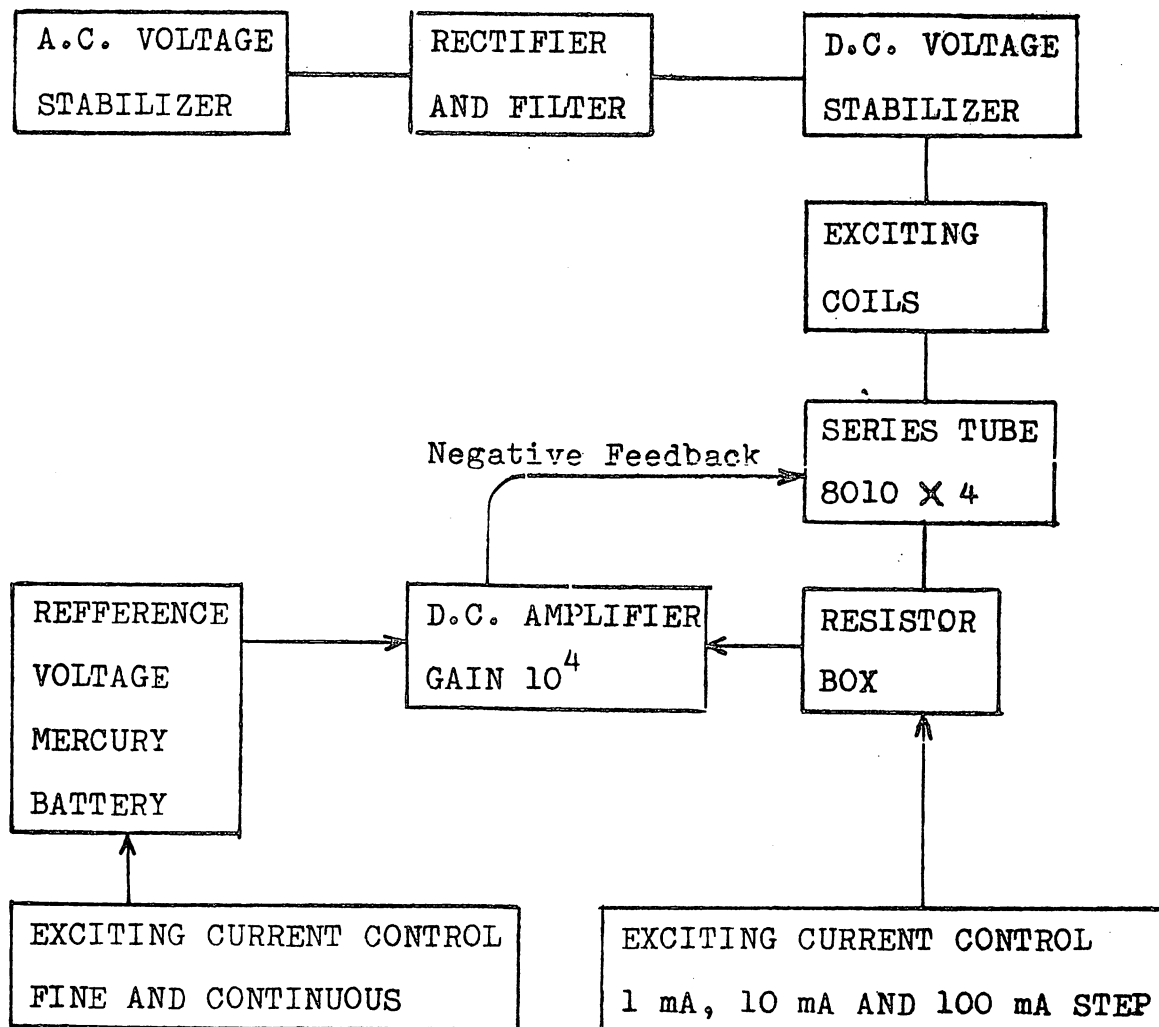


Fig.8. Block diagram of magnet power supply

The exciting current is controlled roughly by changing the standard resistors and finely adjusted by changing the reference voltage.

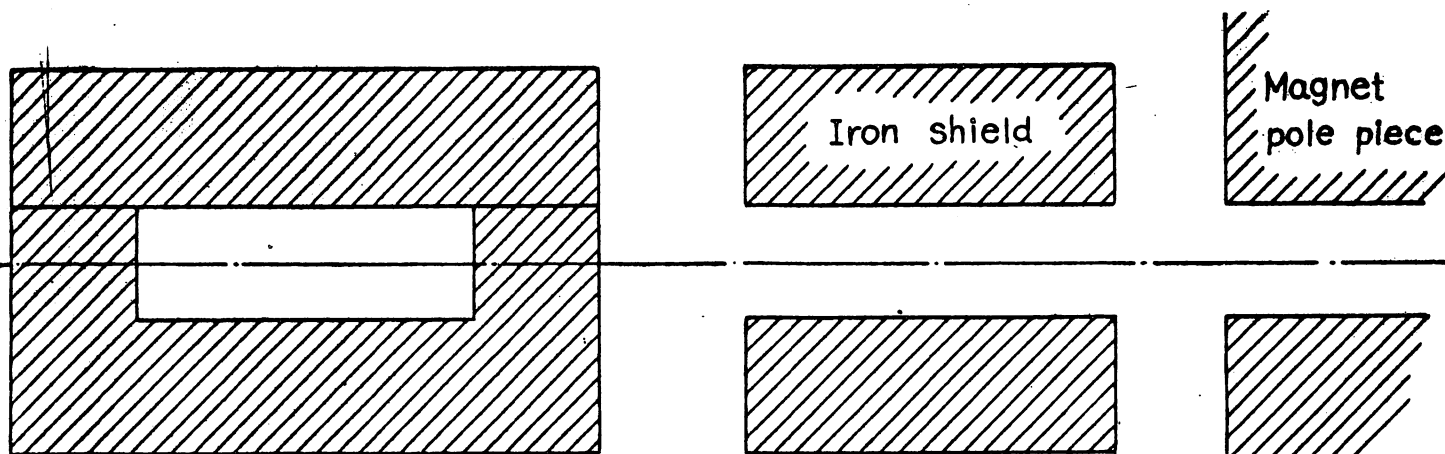
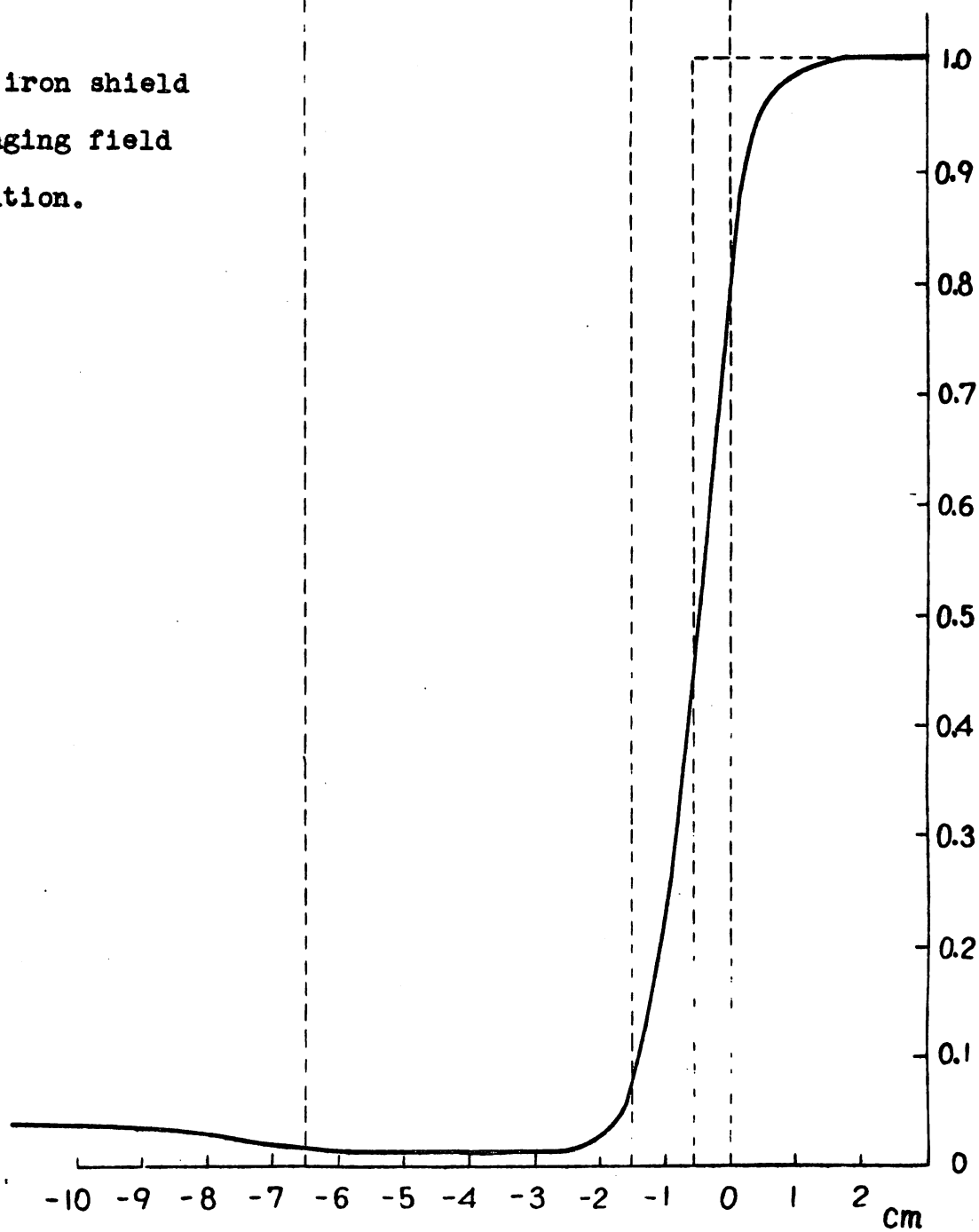
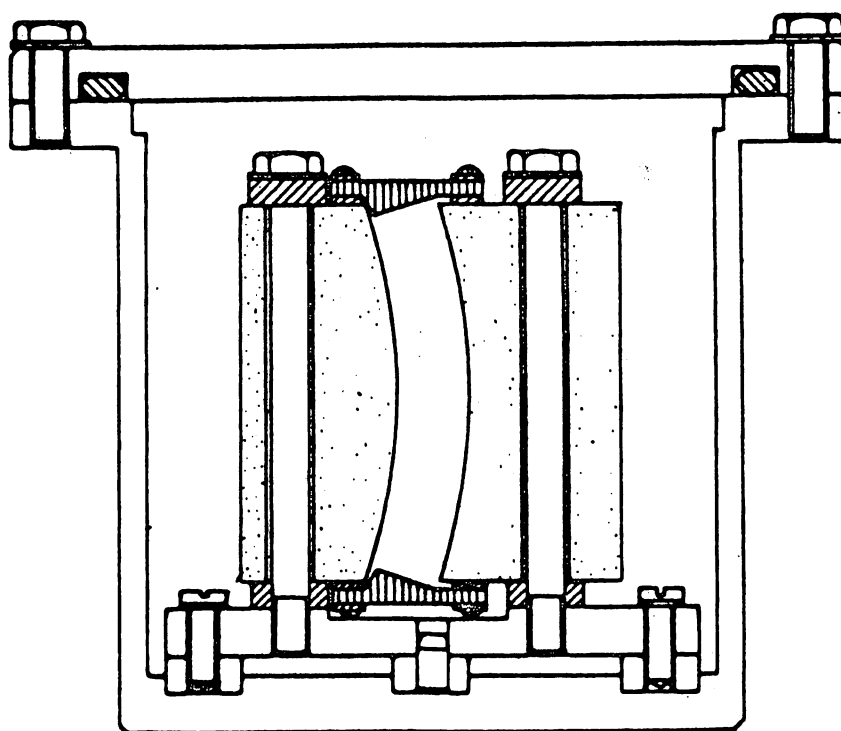


Fig.9. Herzog iron shield
and fringing field
distribution.






	Toroidal condenser		Steatite insulator
	Auxillary electrode		viton O-ring

Fig.10. Cross section of the energy selector

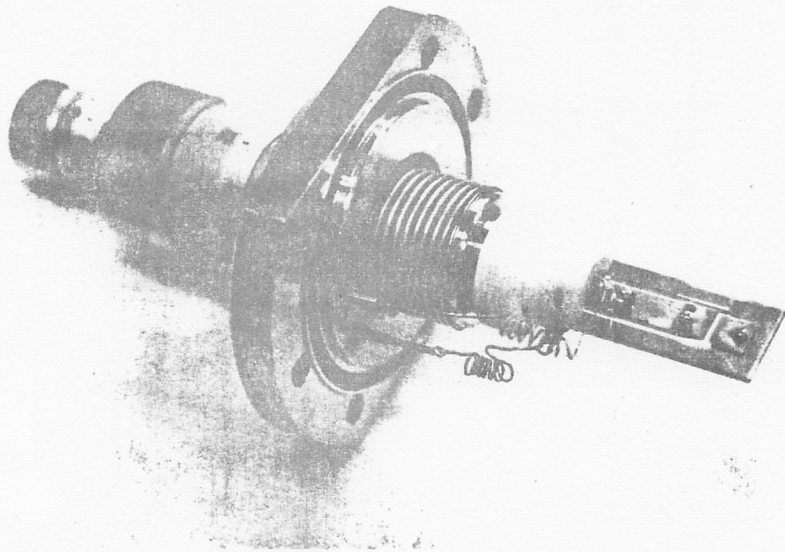


Fig.11. The β -defining slit.

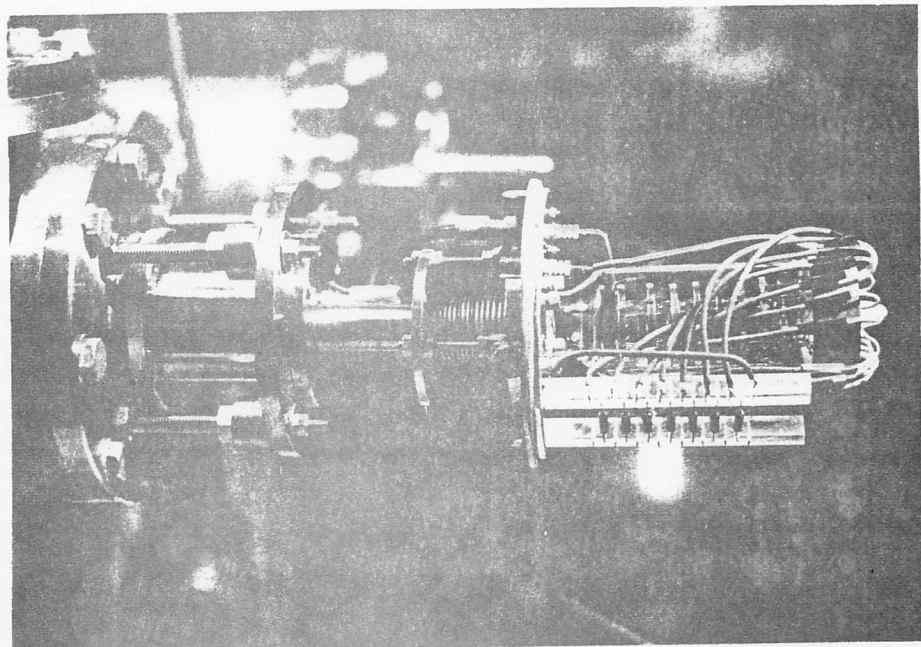


Fig.16. The 15-stage electron multiplier.

1. Herzog iron shield only.
2. Energy selector is shielded with Si steel sheets.
3. Permalloy pipe and iron sheets are inserted additionally.

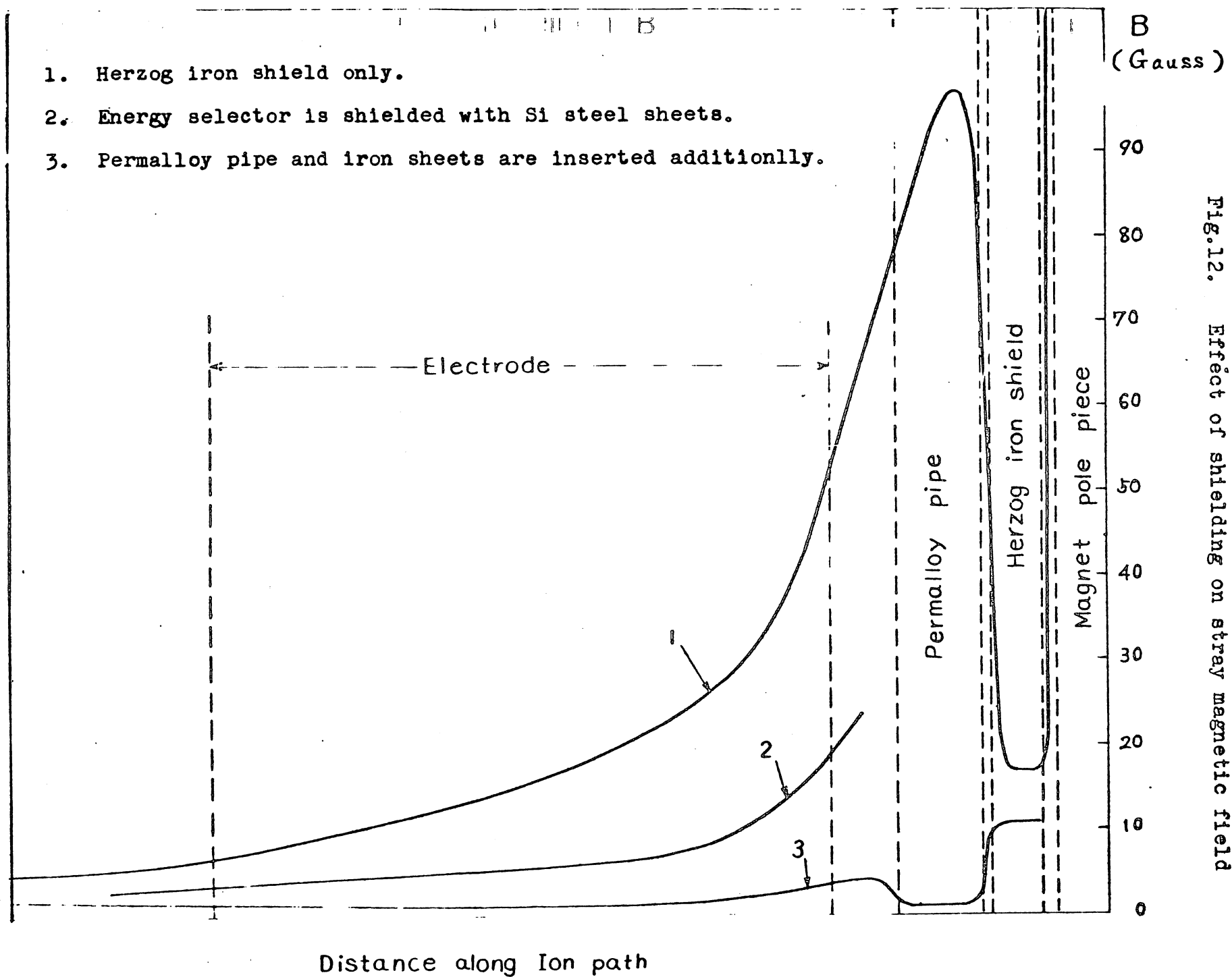


Fig.12. Effect of shielding on stray magnetic field

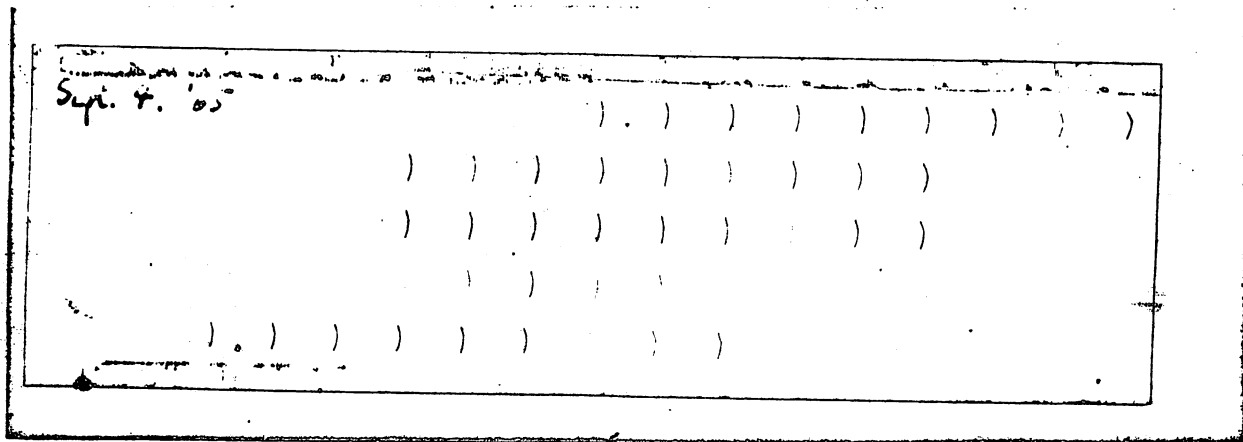


Fig.13. Example of artificial multiplets. (x1)

$^{39}\text{K}^+$ lines are shifted by changing the potential between condenser electrodes. The shifted potential between successive exposures is 1.1 volts and the potential of center line 1776 volts.



Fig.15. Example of improved mass spectral lines. (x5)

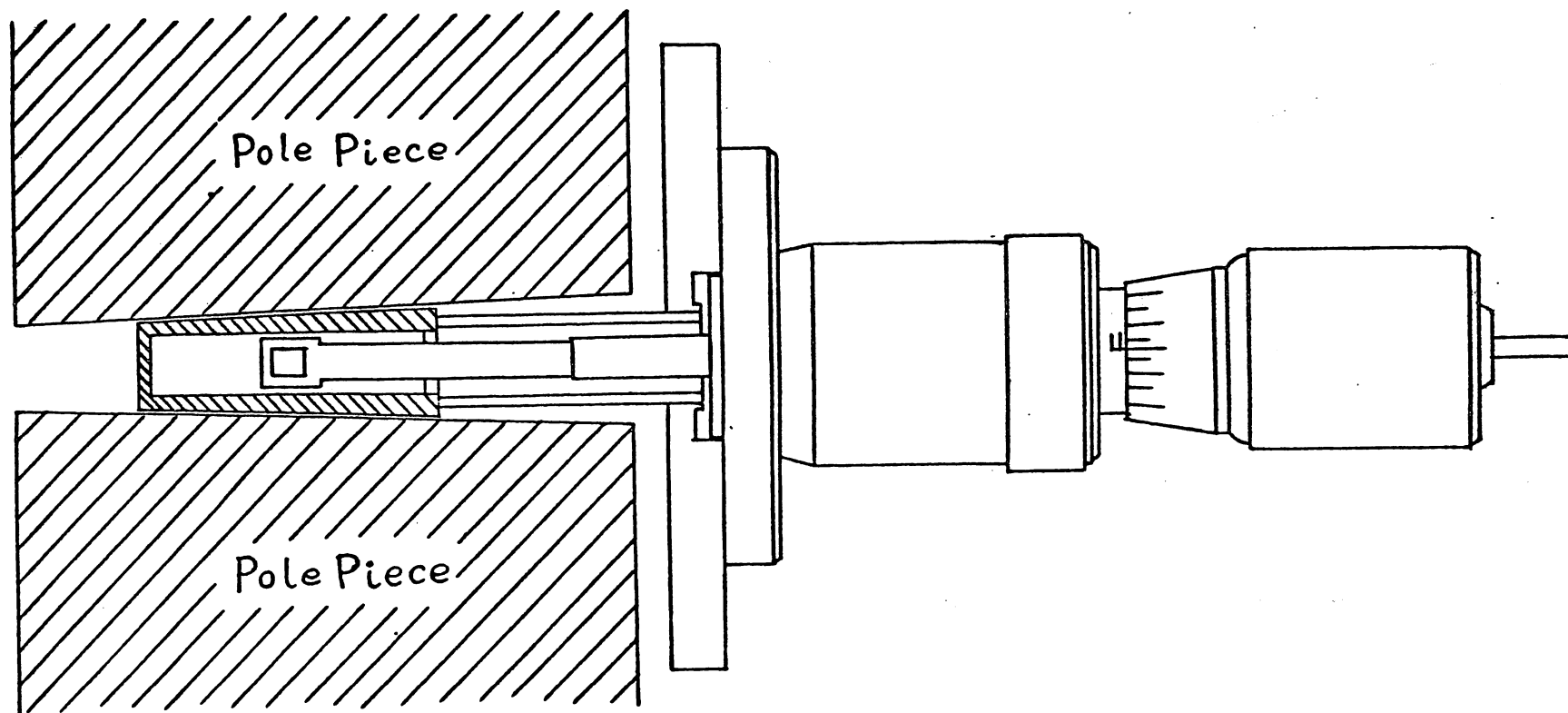


Fig.14. Movable slit in the dispersing magnetic field.

Slit hole dimension: 4 mm X 5 mm

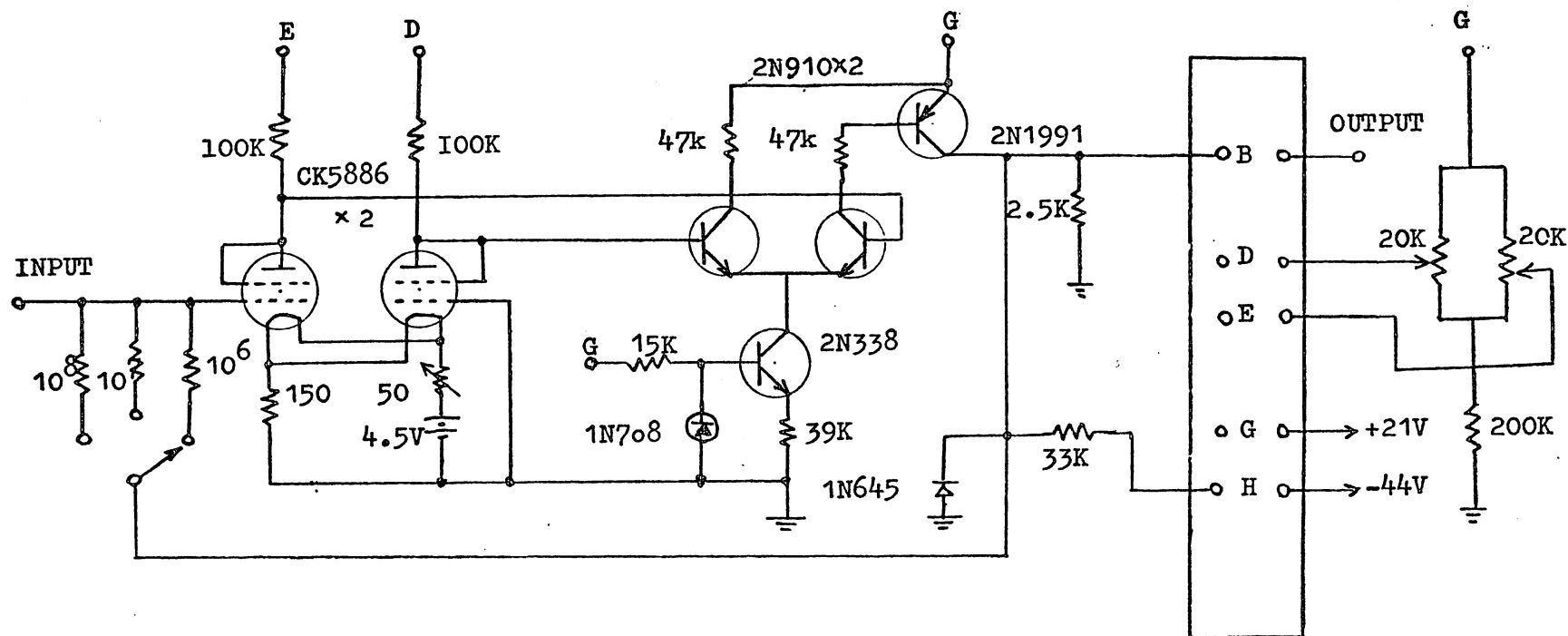


Fig.17 The circuit diagram of the preamplifier.

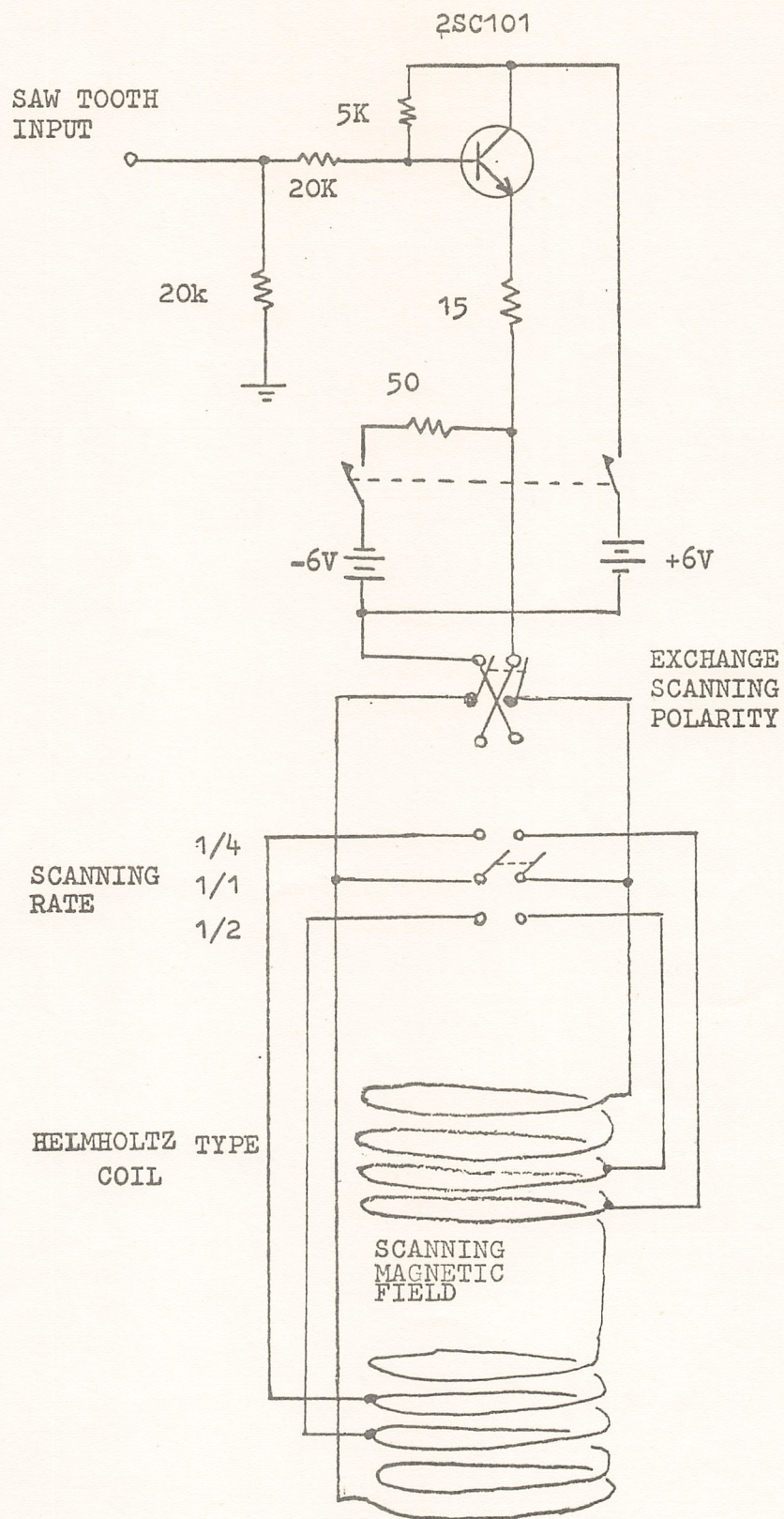
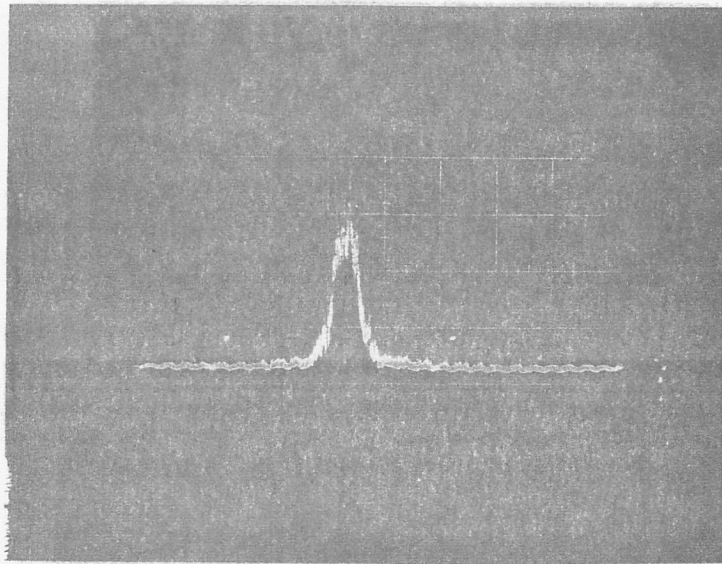
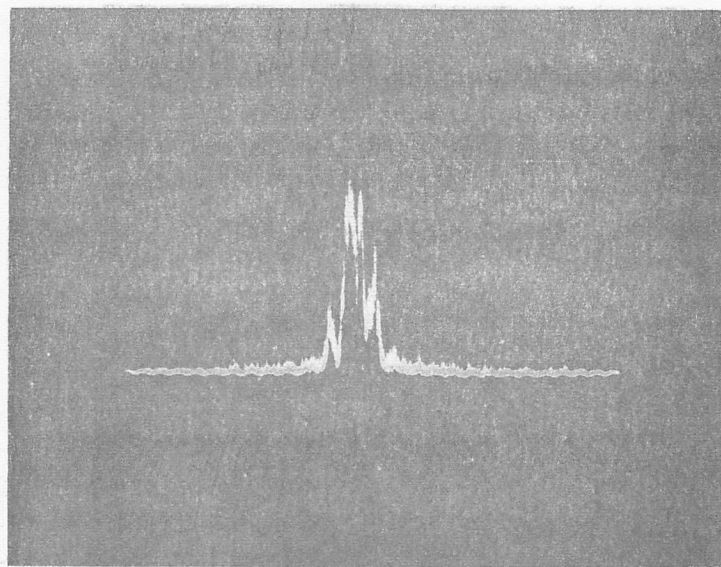


Fig.18. The circuit diagram of the beam scanner.



(a)
b



(b)
2

Fig.19. Cancellation of the 60 Hz hum magnetic field.

(abscissa 50 ms per division)

(a) Mass peak of ⁴⁰Ar is modulated by the hum magnetic field.

(b) Amplitude modulation is much reduced by the cancelling circuit.

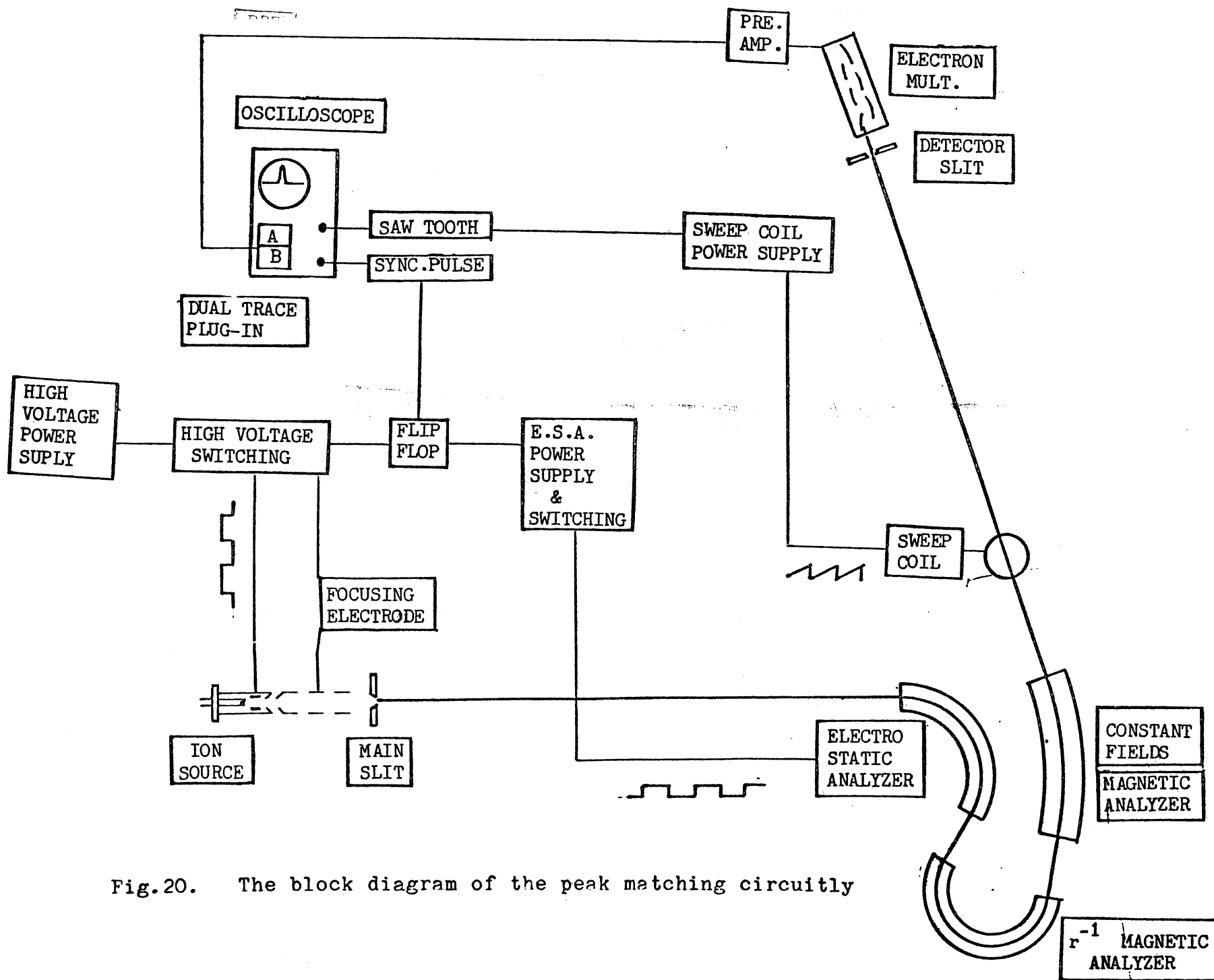


Fig.20. The block diagram of the peak matching circuitly

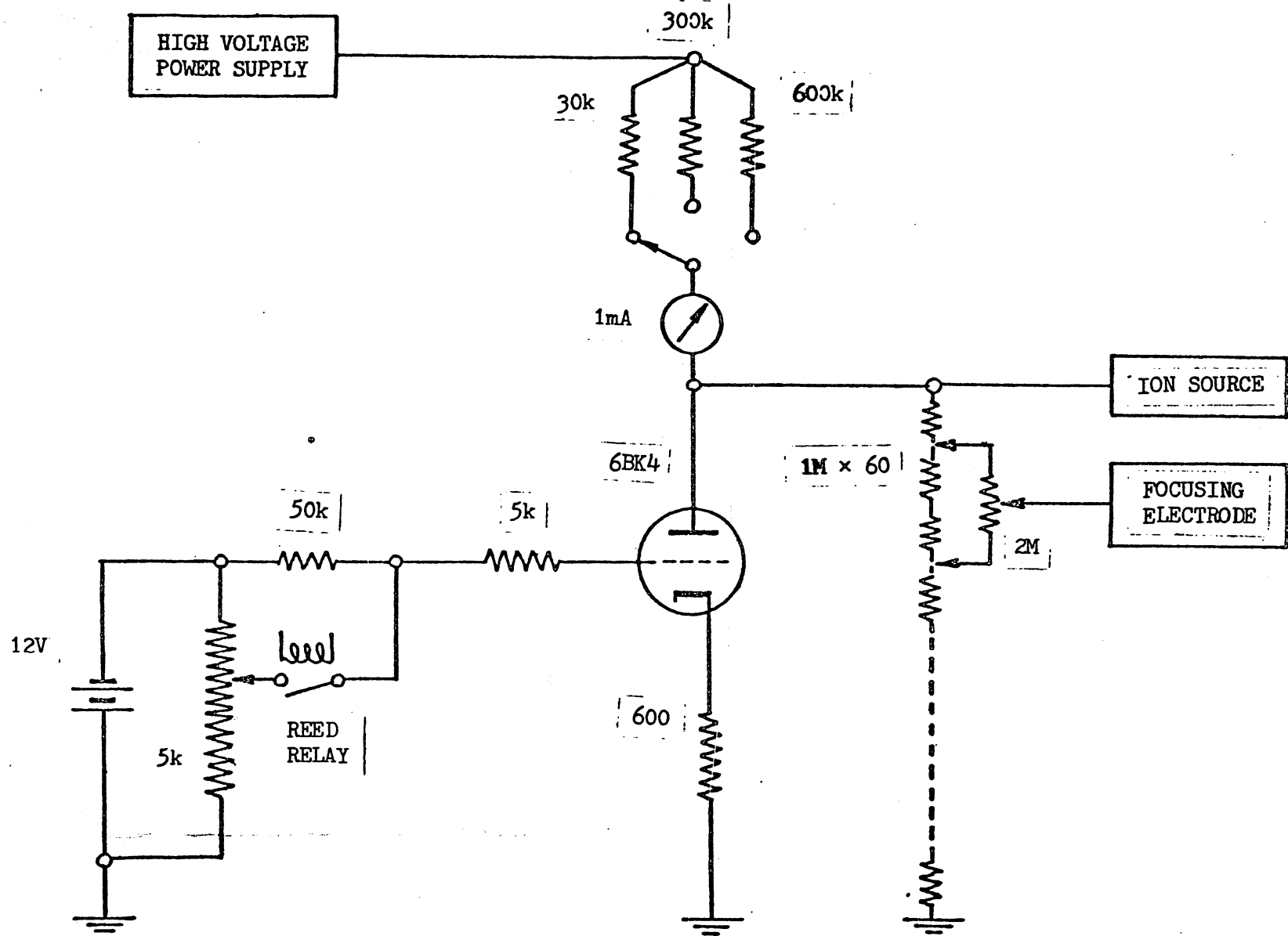


Fig.21. The block diagram of the high voltage switching circuit

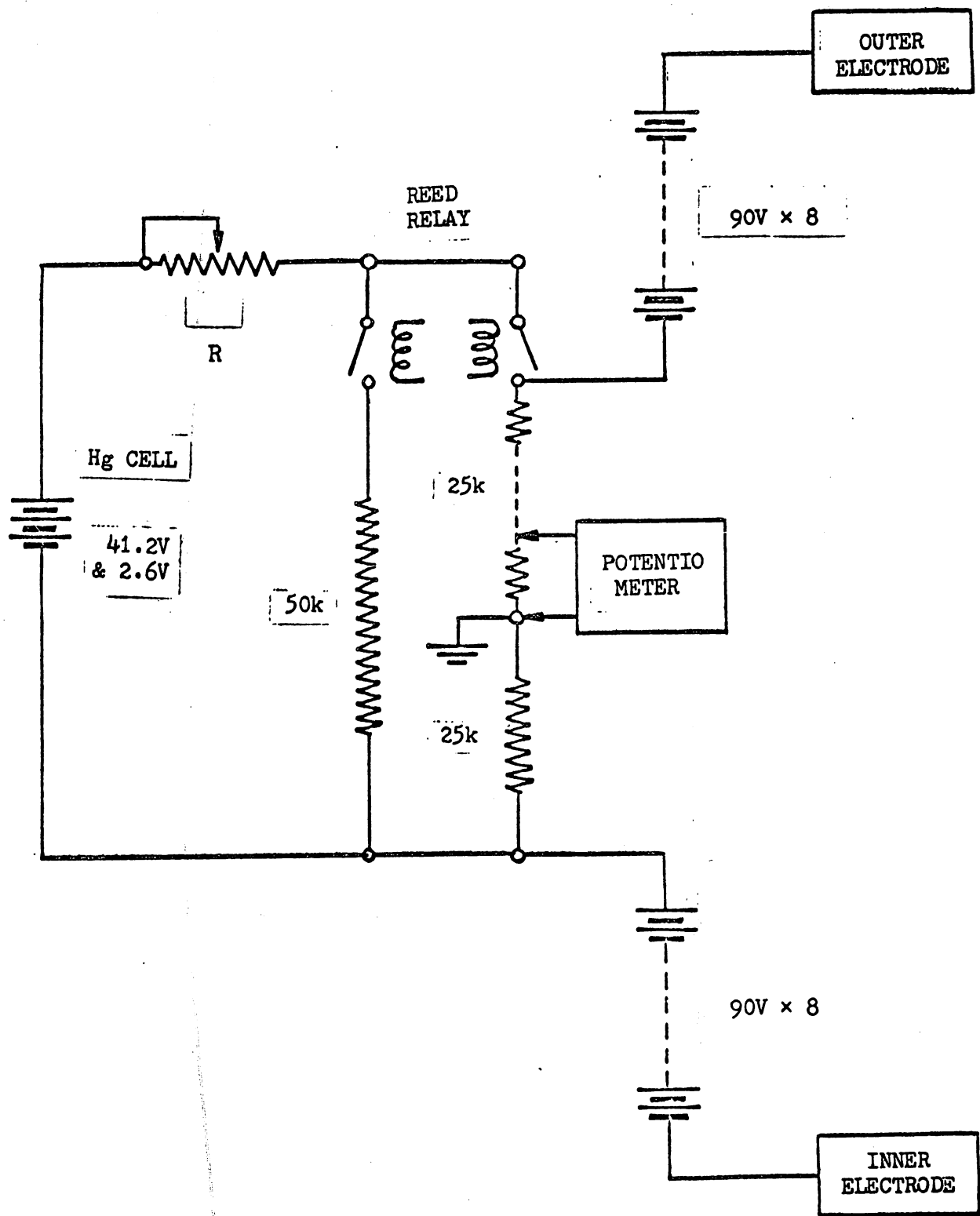
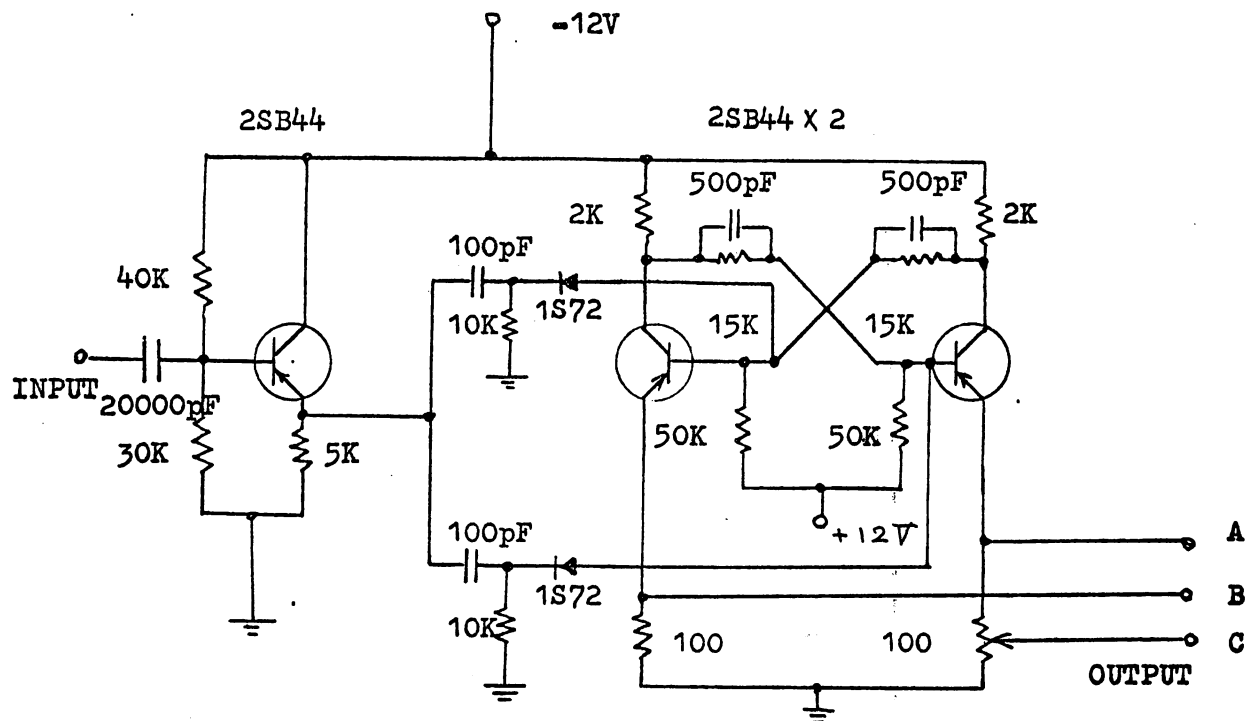
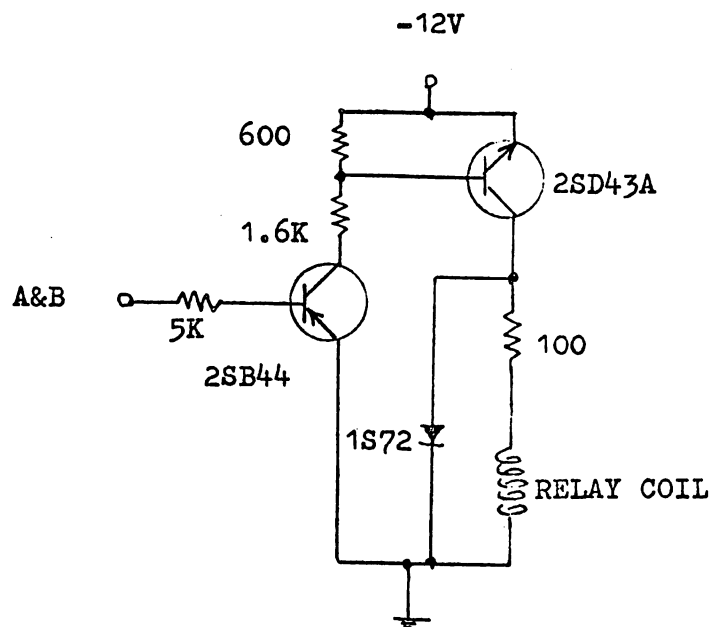


Fig.22. The block diagram of the energy selector power supply



(a)



(b)

Fig.23. The circuit diagrams of the flip-flop (a) and the driver of reed relay (b)

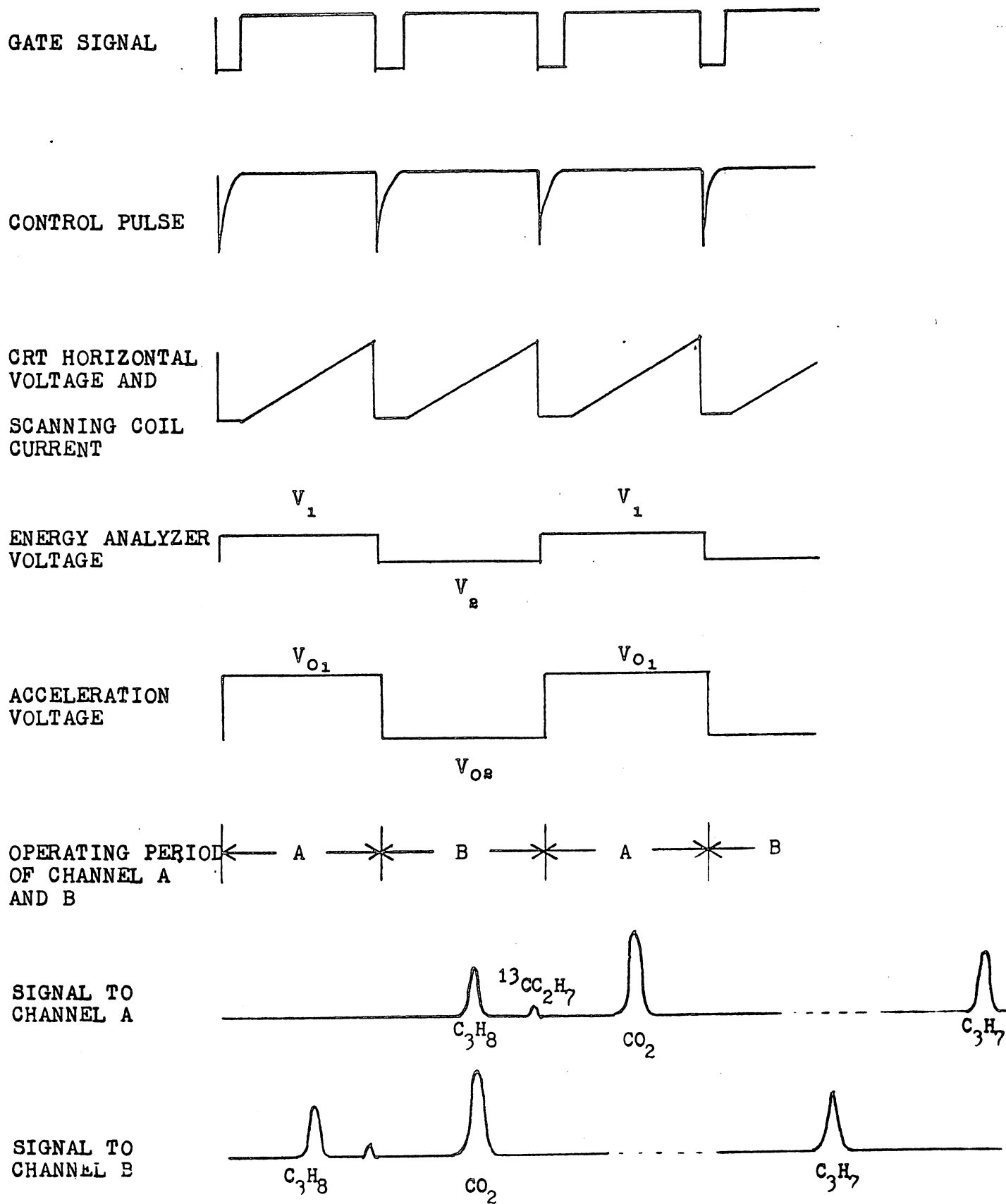


Fig.24.. Phase relationships in peak matching circuits.

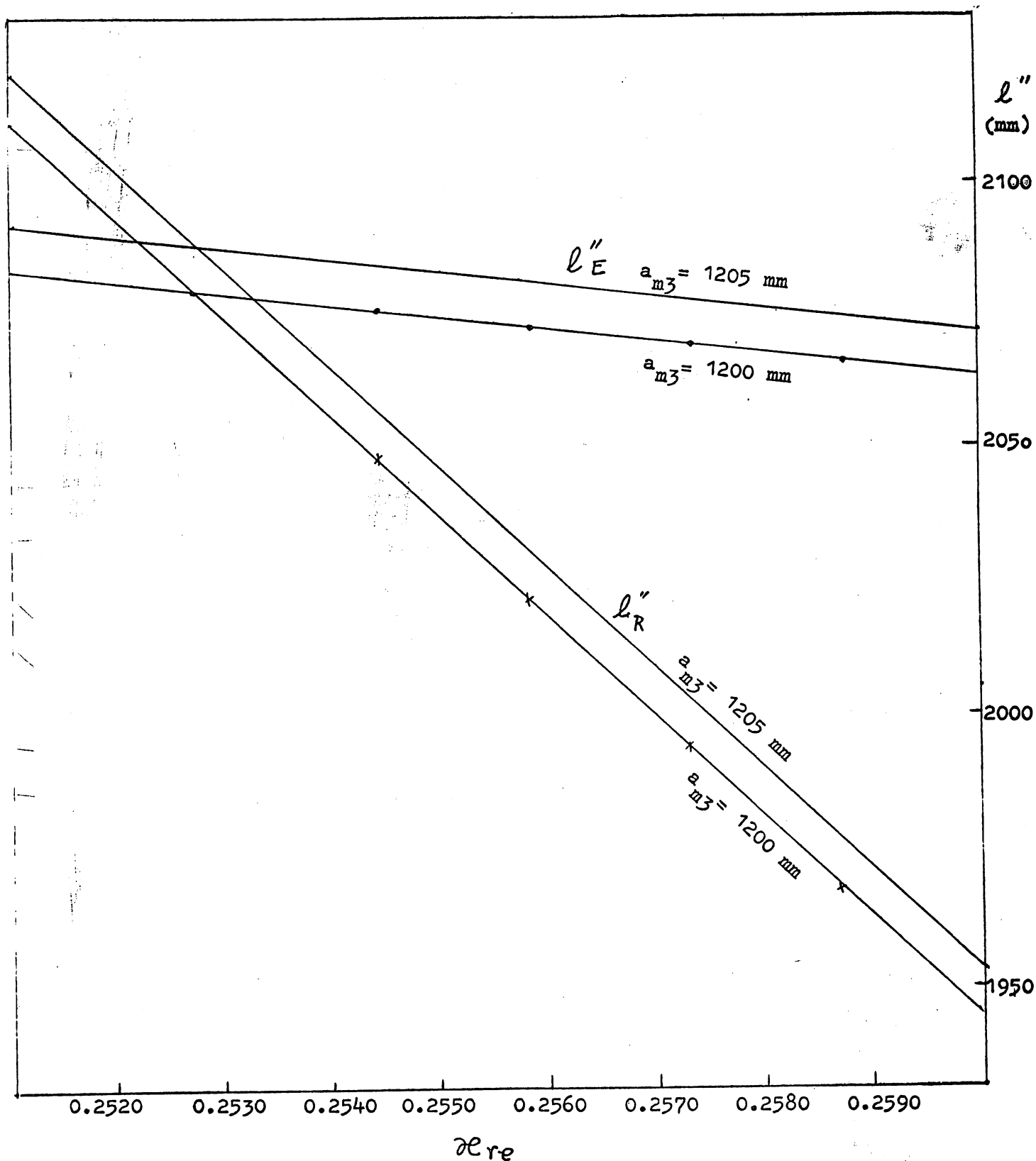
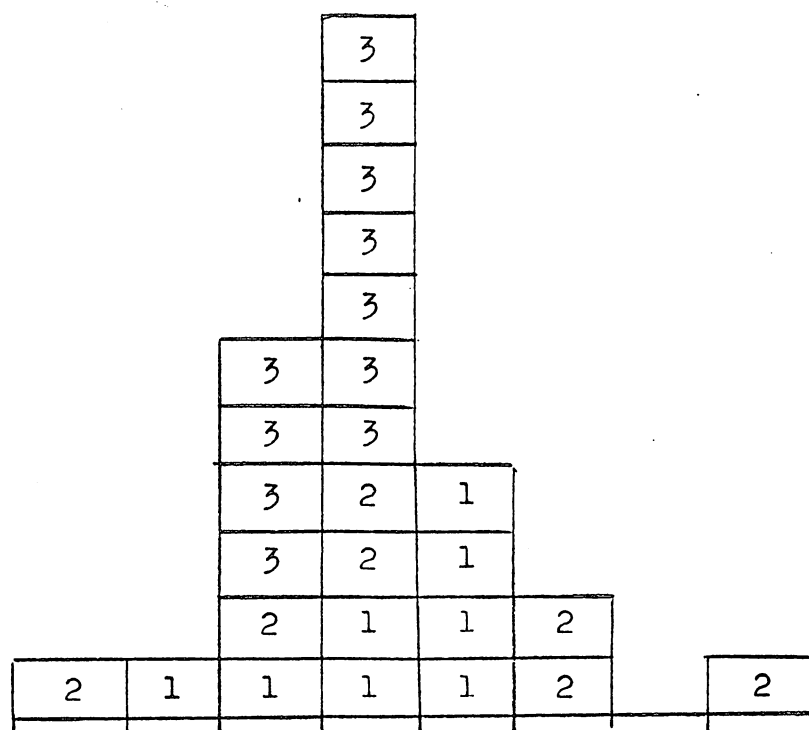


Fig.25. $\partial \ell_{re}$ -dependence of the image distance.

The image distance of the direction focusing l''_R is much more sensitive than that of the energy focusing l''_E .

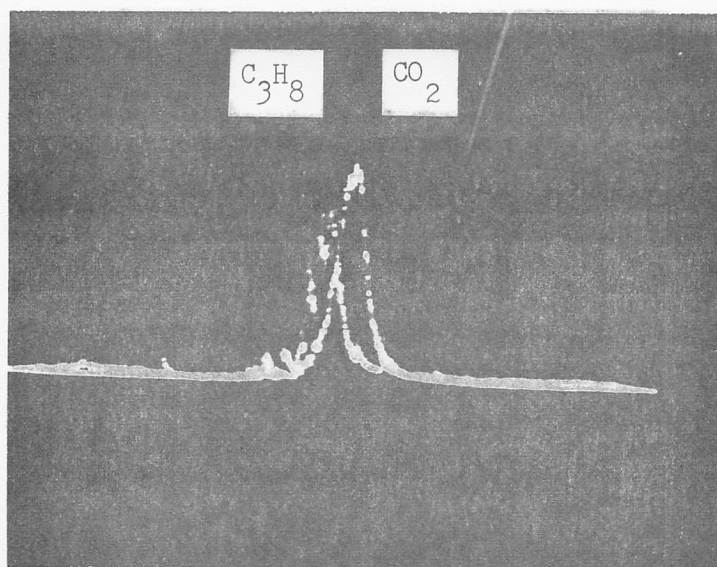


72.74 .75 .76 .77 .78 .79 .80 .81 .82
 Mass differences of $C_3H_8 - CO_2$ in μu

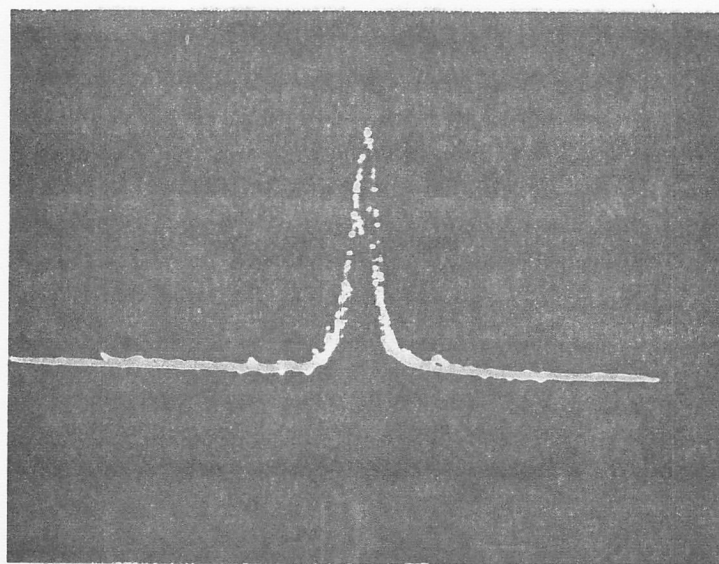
Fig.26. A histogram of 26 values of mass difference $C_3H_8 - CO_2$. Numbers 1, 2 and 3 show the runs of April 25, 1967, May 16, 1967 and May 17, 1967 respectively. They appear to follow a normal distribution. Total spread of results is 68 μu and the probable error representing the reproducibility of the results is 1.7 μu .

Fig.27. C_3H_8 -- CO_2 doublet displayed on CRT.

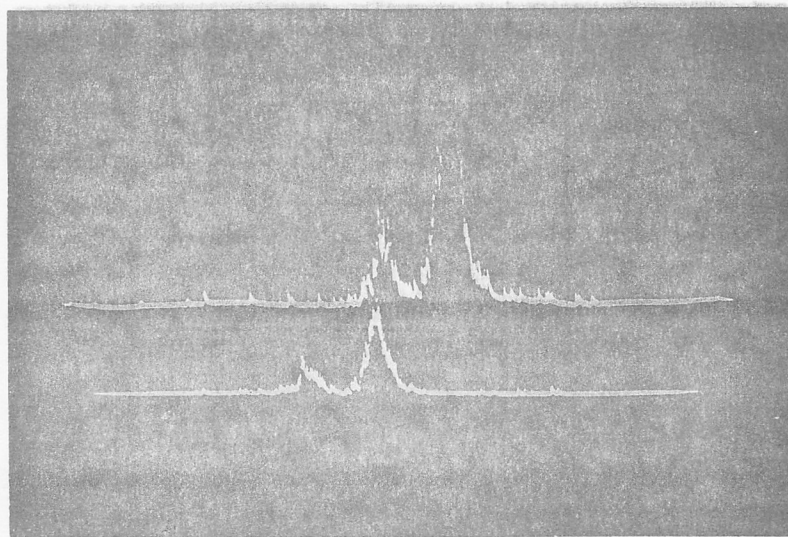
$$\begin{array}{c} \leftarrow | \quad | \rightarrow \\ \frac{M}{\Delta M} = 350,000 \end{array}$$



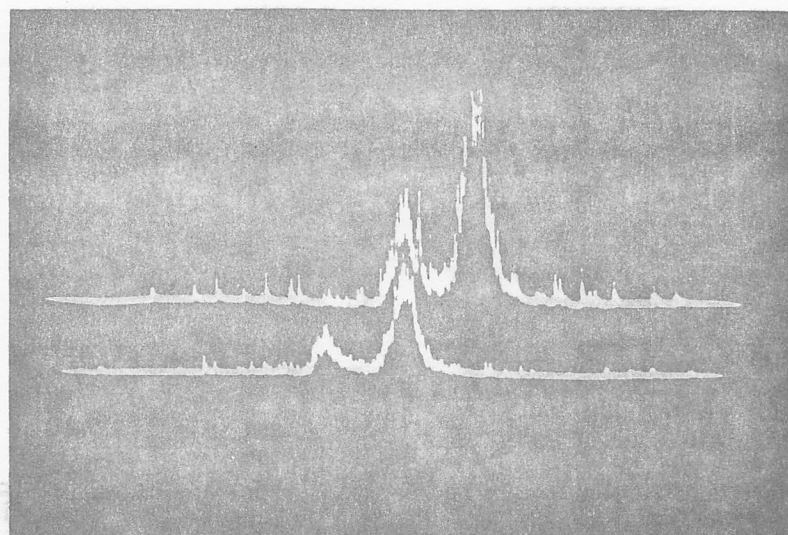
50% MISMATCH



MATCH



(a)



(b)

Fig.28. The oscilloscope patterns of $^{40}\text{Ca} - ^{40}\text{Ar}$ doublet.
 ^{40}Ar peak has higher intensity.

(a) ΔV is set at the value corresponding to mass difference $205 \mu\text{u}$.

(b) The peaks are matched.

